Utrecht University

Department of Physics and Astronomy

Master Thesis

Variance reduction techniques for Monte Carlo simulations of photon transport in liquid xenon detectors

Author:
Olivier Kesber

Supervisors:
Prof. dr. Auke-Pieter Colijn
dr. Stefan Bruenner

Second examiner:
Prof. dr. Raimond Snellings

June, 2020

Abstract

This work is an attempt to improve simulations of background signals in a liquid xenon dark matter experiment. In an experiment such as XENON1T one aims to measure a Dark matter signal. Since such signals have not been recorded, and therefore an effort is made to increase the sensitivity of the experiment. One strategy is by scaling up the experiments and thereby increase the active volume of the experiment. With larger detectors, simulations of background signals become more inefficient and will be computationally expensive. However, with advance variance reduction techniques, it is possible to improve the simulation efficiency by three orders of magnitude. This project is centred around one of such a method and provides insight into the working of the method as well as the validation thereof.

Chapter 1 presents an introduction into dark matter and the experimental evidence to support the dark matter hypothesis. Chapter 2 describes the XENON dark matter experiment and the working thereof in more detail. Chapter 3 provides a description of gamma-ray transport and interactions in matter. Chapter 4 introduces an MC method to simulate gamma-rays in a liquid xenon vessel. In chapter 5, a paper is presented that is the result of this research and gives an accurate description of the accelerated MC techniques. Lastly, a conclusion and discussion are provided in chapter 6.

Contents

Chapter 1

Dark Matter

Dark matter is one of the biggest mysteries of modern physics. It forms a missing link between the understanding of the universe and the observations we make. This missing piece of information may hold a treasure of new physics. A mere glance of a dark matter particle would be one of the biggest discoveries of our time since it would be the first particle that is not part of the standard model. On the other hand, not detecting anything would also have large implications on our understanding of the universe since in that case, our laws of gravity might be wrong. So something worth investigating. This chapter will show where the dark matter hypothesis comes from and show experimental evidence for dark matter in our universe. Furthermore, some candidates and detection strategies will be introduced.

1.1 ΛCDM Model

Our current best understanding of the universe is described by the Big Bang model. This model arises from Einstein's theory of general relativity and gives an accurate description of the cosmic microwave background, large scale structures, abundances of light elements and the accelerating expansion of the universe. Besides the model, there is striking experimental evidence that our universe is flat and uniform [1]. Combining these experimental results with the existing theory the following equation for the energy density of the universe can be derived[2].

$$\rho(t) = \rho_{cr,0}(\Omega_{R,0}a(t)^{-4} + \Omega_{M,0}a(t)^{-3} + \Omega_{\Lambda,0}) \tag{1.1}$$

Where a is the time dependant scale factor of the universe with the present day value of $a_0 = 1$, and $\rho_{cr,0}$ notes the current critical density. But the central information is the ratio between the three different energy densities as they are today of: radiation $\Omega_{R,0}$, matter $\Omega_{M,0}$ and dark energy $\Omega_{\Lambda,0}$. This yields an odd issue since the expected density of matter $\Omega_{M,0}$ is approximately equal to 30% of the total ,while the ordinary matter, only makes up about 5% of the total density [1]. This discrepancy suggests that there should be an additional 25% density comprised of an unknown (non-relativistic) substance that does not interact with light. Hence the introduction of (cold) dark matter (CDM). (see table 1.1 for the exact values of the Ω_i). Another fascinating figure in this table is the density of the dark energy. This "substance" that makes up the majority of the energy in the universe is even more elusive than dark matter but will not be covered in this work. To summarize: the universe is best described by a model in which most of the energy is made up out of dark energy Λ and cold dark matter CDM.

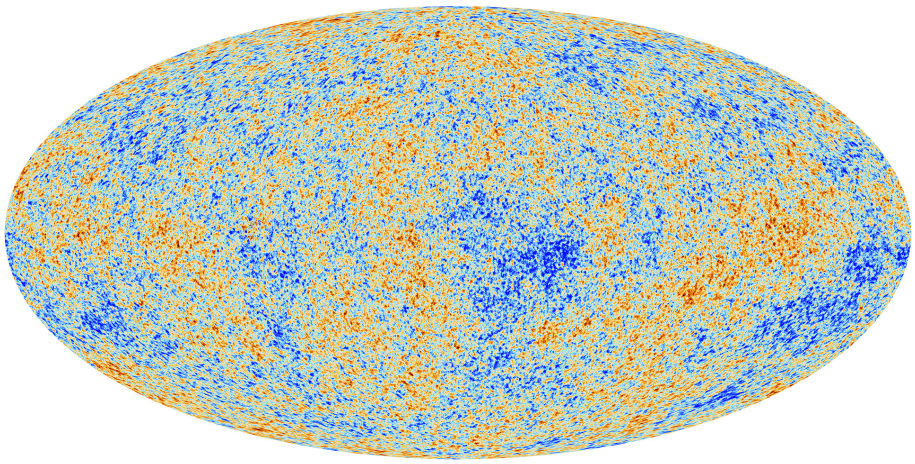

Figure 1.1 – Temperature fluctuations in the CMB as seen by the Planck Telescope. The visible features (blue and red) are fluctuations on the scale of 100-200 micro kelvin. The overall temperature is 2.72548 ± 0.00057K [1]

1.2 Experimental evidence for Dark Matter

The Dark Matter(DM) hypothesis can be tested on vastly different scales, namely (1) on the level of the universe through the Cosmic Microwave Background (CMB), (2) on the scale of galaxies clusters, and (3) at the size of galaxies.

1.2.1 Cosmic Microwave Background

Very striking evidence for the existence of DM is the accurate description of the CMB and its features. The CMB is the oldest light in the universe which was sent out 380.000 years after the big bang. The most recent measurement of the CMB, made by the Planck telescope [1], is shown in figure 1.1. In general, the temperature of the CMB shows the expected black body spectrum. However, tiny temperature fluctuations at the $100 - 200\mu$K scale are present. These fluctuations hold valuable information and therefore are an excellent feature to check if a model with DM can describe them. To do this, the angular distribution of these fluctuations are decomposed them into spherical harmonics. Figure 1.2 shows the spectrum of the temperature fluctuations of the CMB, as a function of multipole moment l.The power spectrum is used to fit the ΛCDM model parameters. With these fitted parameters that are shown in table 1.1, the ΛCDM is able to produce a model that is in agreement with the power spectrum.

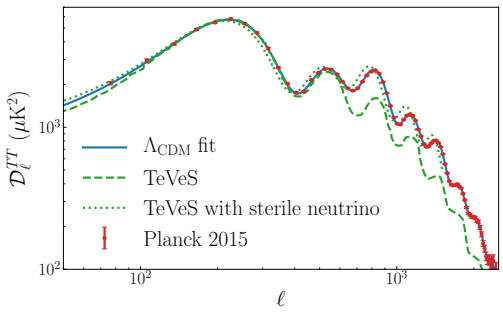

Figure 1.2 – The spectrum of the anisotropies in the CMB as a function of the multipole moment l. The points with errors represent the measured point by the Planck collaboration [1], and the blue line express the ΛCDM model [3]. The two green lines represent an alternative model that is based on modified gravity [4][5]. (From [6] [7])

	Symbol	Value
Dark energy	Ω_Λ	0.6911 ± 0.0062
Dark matter	Ω_{DM}	0.2589 ± 0.0057
Baryonic matter	Ω_m	0.0486 ± 0.0010
Radiation	Ω_r	8.24×10^{-5}

Table 1.1 – The energy densities from the different components as measured by the Planck telescope. Please take a moment to note that the baryonic matter only makes up less than 5% of the total universe. The radiation density represents the relativistic particles so cosmic radiation and neutrinos. Data is available at [1]

1.2.2 Large scale structure

Besides on the scale of the CMB, there is evidence for the presence of dark matter on the scale of the cosmic web as well with the two primary distinct pieces of evidence: (1) DM can very well explain the observed structure in our universe, and (2) there are certain specific features on the scales of galaxy clusters that can very well be explained with DM. Our universe is incredibly uniform, however it is intuitively understandable that regions with higher density will form due to gravitational effects. Yet, the level of attraction is highly dark matter model dependant since ordinary matter exerts an outward pressure, whereas dark matter does not exert such an outward pressure. Therefore, a universe with only baryonic matter will not be able to form the large scale structures that are measured by astronomical observations [8]. Besides the sheer existence of large scale structures, there is specific evidence for the DM hypothesis. Namely, a phenomenon called gravitational lensing and a specific observation of the Bullet Cluster. Firstly, (weak) gravitation lensing occurs when there is a large mass (a cluster) in the line of sight of the observer and the object that is observed. Due to the gravitational potential between the object and the observer, the image is distorted. Because dark matter also exhibits its own gravitational potential, it can contribute to lensing effects. Detection can than happen in by either observing a strong lensing effect from a body with little baryonic mass or observe a lensing effect from regions where there is hardly any baryonic matter [9].

A specific example of the latter is the Bullet Cluster. It is assumed that 2 collided galaxy clusters form the Bullet Cluster. These galaxies clusters consisted of stars and interstellar gas, of which the latter makes up most of the total (normal) mass. When the galaxies hit each other, it is assumed that the massive gas clashed, but that the stars mostly missed each other and flew passed each other. This resulted in two clusters that are stripped away from their gas clouds. These clusters are then expected to be much lighter and that most of the mass is located in the combined gas cloud. However, this is not what is observed. Making use of several different observation techniques, it is possible to measure the mass density of the different regions of the cluster. A picture of the Bullet Cluster is shown in figure 1.3, where it is shown that most of the mass is located in the less luminous star regions of the galaxies. That is, it is not located as expected in the massive gas cloud. The presence of dark matter could elegantly explain this phenomenon. If one assumes that most of the mass in the clusters is in the form of dark matter and that dark matter has a

Figure 1.3 – A picture of the Bullet Cluster made by the Hubble and Magellan optical telescopes. The gas cloud is observed by the Chandra X-ray observatory and is illuminated pink. The mass density is determined using gravitational lensing and is coloured blue.[11]

very low cross-section, it would explain this cluster entirely. This is done by realizing that the dark matter will fly through the other cluster unaffected and therefore taking most of the mass to the less luminous star region [10].

1.2.3 Rotation curve

The dynamics of stars in the galaxies is a piece of strong evidence for the dark matter hypothesis. The scale of galaxies is also the smallest scale where the (gravitational) anomalies, possibly due to dark matter, are observed. The discrepancy occurs in the spiralling motion of stars in a galaxy. The laws of Newton and Einstein provide us with a good understanding of such stellar movement. Given these theories, there is a relation to the total mass of the galaxy and the velocity of an object around the galactic centre (Kepler's law).

$$v_c(R) = \sqrt{\frac{GM(R)}{R}} \tag{1.2}$$

Where $v_c(R)$ is circular rotation velocity of an object at a distance R from the galactic centre and G is the gravitational constant and $M(R)$ the total mass within in a sphere of radius R from the galactic centre.

R and $v_c(R)$ can be measured using astronomical observations, there results are shown in figure 1.4. Because we can measure the mass of the stars and gas in the galaxy, we can estimate what $M(R)$ is and model what the circular rotation velocity of objects should be according to equation 1.2. As seen in the plot, the models do not provide an accurate description of the data. For a distance, these models follow a $1/\sqrt{R}$ distribution whereas the data indicate an increasing trend (also for large distances). This oddity could be resolved by the introduction of the so-called dark matter halo. Briefly explained: this

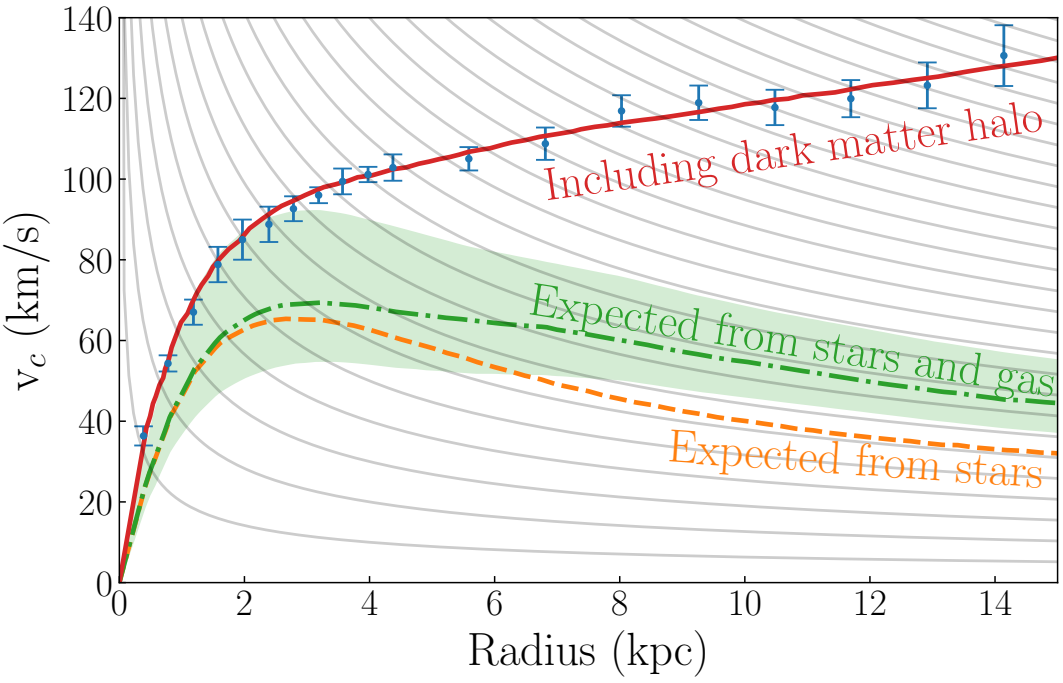

Figure 1.4 – The rotation curve of M33 galaxy, measured using the Doppler shift from the 21 cm radio emission of atomic hydrogen. The expected curve from the stars with and without including interstellar gas in the model are shown in green and orange. The band show the systematic uncertainties on the model. The grey background lines represent a $1/\sqrt{R}$ relation (expected behaviour for large radii). The data points (Blue) clearly do not flow this trend but are in a better agreement with the halo model that includes a large unseen mass component (DM). Data from [13]. (From [6] [7])

model describes the dark matter in the galaxy as large spherical halo where the density scales with $1/R^2$ with a hard cut of at the edge[12].

1.3 DM candidates

It is established in the previous section that the ΛCDM model gives an accurate description of the universe by explaining the missing mass through the introduction of dark matter. Using this "simple" solution to the problem gives rise to a "complex" enigma: what is dark matter made of? We can exclude all known standard model particles. Either on terms of (colour)charge (quarks and charged leptons) or on their mass (neutrinos are to light and take up to much phase space to make up the expected densities) [14]. Therefore a theory beyond the Standard Model is necessary to predict possible candidates. There are numerous theories for such an extension.

1.3.1 WIMPs

One of the most studied dark matter candidates is the so-called Weakly Interacting Massive Particle (WIMP). These WIMPs are "weakly interacting" since they are expected to have interactions that are at the order of the weak scale, but the interactions do not have to be mediated by the weak force. The particle must be a "massive particle" since it must have a sufficient mass to solve the discrepancies between the theory and the astronomical observations. There are several compelling reasons to consider WIMP as a valid DM candidate. (1) The production mechanism of such a WIMP is well understood and gives a convincing explanation for the abundance. (2) It is predicted to exist in a range of beyond

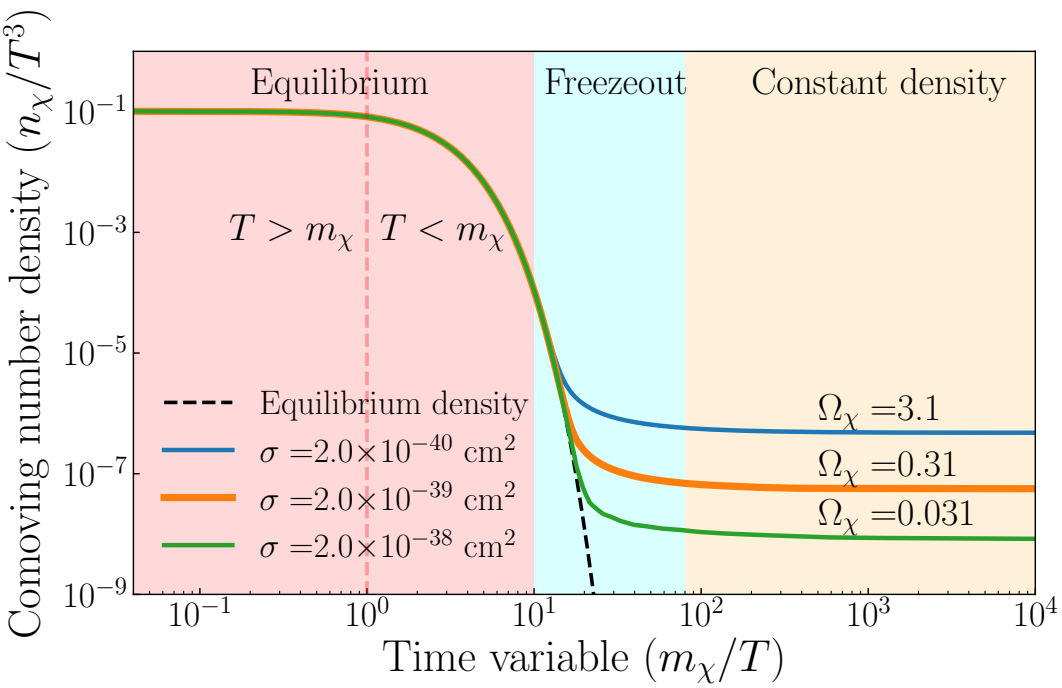

Figure 1.5 – The number density n_χ of dark matter particles χ, the n_χ/T^3 is used to compensate for the expansion of the universe (scale proportional to T^{-1} and for the same reason the m_χ/T can be used as a time variable. At the early times, equilibrium is reached due to reaction rate compared to the expansion of the universe. When the temperature drops below the mass of the WIMP mass, the production stops and the density is no longer in equilibrium. At Freezeout region the annihilation rate also drops. The start point of this freezeout depends on the annihilation cross-section and is shown by the 3 different lines. After this freezeout, the annihilation stops, and the number density remains constant. The $\sigma = 2.0 \times 10^{-39} cm^2$ cross-section line gives a density that is in the right order of magnitude that is observed. (From [6] [7])

the standard model theories [15]. (3) It is a hypothesis that is testable since one can study the "weak" interactions.

As mentioned, there is a good hypothesis where WIMPs originate from. The most popular explanation is called the "freeze-out" or decoupling [16]. This mechanism states that within the first nanosecond of the universe, the number density was very high and all particles were in thermal equilibrium, i.e. there was enough energy available to convert between different particle species ($T > m_\chi$). This extremely hot state was not long-lived due to the expansion of the universe. Due to this expansion (and subsequent cooling $T < m_\chi$) the production rate fell. However, the annihilation rate would be influenced less by the expansion. The unbalances in the creation and annihilation rates would continue until the density becomes low enough to reduce the annihilation probability to effectively zero reaching a new "equilibrium" level that is only lowered by the expansion of space. This means that the abundance of dark matter today is highly dependent on the annihilation cross-section. The cross-section abundance relation can be read from figure 1.5.

1.3.2 Alternative DM candidates

In this chapter, the majority of the information is about WIMPs, since they are one of the most promising candidates to solve the DM problem. However, there are many alternatives to the WIMP hypothesis. Some of them propose a different object to account for the missing mass. But as mentioned, it could also be that the current understanding

of gravity is not complete and need to be modified.

Alternative models are proposed that explain the missing mass by altering or extending the current laws of gravity. These (new) models are called alternative gravity theories, and most popular ones are modified Newtonian dynamics (MOND). Most of them aim to explain the dynamics in the universe without the need for dark matter (or much less; [17]). These theories have recently got attention due to the lag of experimental evidence for DM particles. However, it is very challenging to reconstruct or extend a theory that is as well tested as general relativity. In the future, this explanation will need some breakthroughs in order to continue as a viable option.

Besides WIMPs, other proposed objects could make up part of the missing mass. Most famous are the QCD Axions and Sterile neutrinos. Both of them are proposed by theories that aim to solve other problems (strong-cp problem for axions, and the chirality problems for neutrinos) but could fit the dark and massive requirements [18][19]. Yet, both of them have not been observed, and therefore they remain as elusive as WIMPs. Besides fundamental particles, it is also proposed that dark matter is made up of MAssive Compact Halo Objects (MACHOs). These astronomical bodies consist of baryonic mass but are hard to detect because they are not luminous. Because this theory did not need to introduce new undetected particles, it was considered a favourable option. Nonetheless, it has lost popularity since recent results have experimentally excluded this possibility. [20]. Furthermore, another astronomical dark matter candidate are primordial black holes. This is still a viable option, but the constraints on the mass of the black holes are increasing by new observations and only leave a few windows open. On the other hand, a recent back hole merger seen by the LIGO fits in one of these windows and therefore proves that such black holes exist [21]. Lastly, besides cold dark matter models, "hot" and "warm" dark matter models exist. Hot Dark matter models propose a particle similar to the WIMP but with the difference that it is an ultra-relativistic particle. Such ultra-relativistic particles must have very low masses, and therefore would offer a feasible explanation why WIMPs haven't been detected. On the downside, it is hard to explain the structure in the universe with only hot dark matter. Warm dark matter theories live in between the hot and the cold dark matter models. Possible candidates for this type are gravitinos and wimps that have not been created thermally.

1.4 Detection strategies

As demonstrated in this chapter, there is clear evidence for the existing of dark matter and that the WIMP is a prime candidate. To test the dark matter hypothesis, there are 3 different strategies (see figure 1.6a).

The first method is by producing dark matter. In theory, it is possible to create dark matter particles in collision experiments such as the LHC [22]. The most significant limitation is on the weight of the particle. Since a particle collider has an upper limit on the mass of the produced particles (due to kinematics) and they have a lower limit due to energy resolution of the detector [23].

The second method is by looking at gamma-rays (or other cosmic rays) that can be created by dark matter particle-antiparticle annihilations ($\chi\chi \rightarrow \gamma\gamma$). This is done by experiments like AMS-02[24] and IceCube [25]. One expects these signals to be highest in regions with a high dark matter density, like the centre of galaxies or the middle of the Sun[1]. Due to

[1]Because one expects that WIMPs scatter of nuclei in dense regions and thereby losing energy afterwards, the WIMPs can become gravitationally bound. After which the WIMP could scatter again and fall to the centre. As the influx of WIMPs is constant, the caught WIMPs accumulate at the core [26]

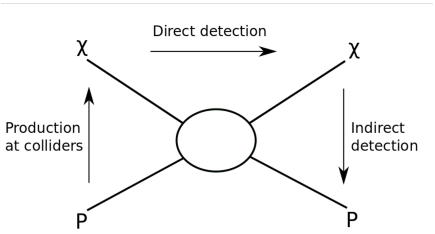

(a) Detection channels of DM searches [23]

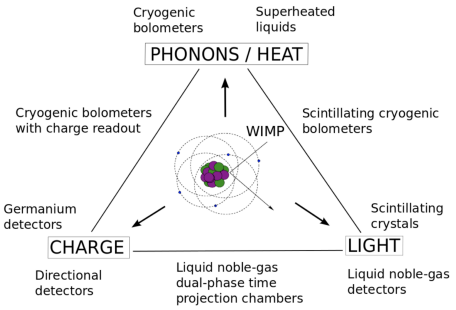

(b) Schematic of direct detection signals and technologies used to measure them. Technologies that measure two signals are placed in between the signals.[23]

Figure 1.6

this strong dependency of local density and astrophysical uncertainties, it is hard to set striking limits on DM as shown by the Fermi-LAT telescope [27]. This detection channel is called indirect detection.

The third method is called direct detection and looks for interaction between WIMPs and ordinary matter. These interactions are assumed to leave a fraction of the kinetic energy of WIMP behind in the material what can be observed through three different signals depending on detector technology. These signals are in the form of heat, light from (de)excitation, and signals from ionisation of the target. Most experiments detect a combination of two of the signals because it provides more information about the interaction, but some others focus on a single signal. [2][23]. See figure 1.6b for a scheme of the detection signals. Liquid noble-gas dual-phase time projection chambers is a strategy to detect both the excitation as the ionization signal and is used by the LZ collaboration [28] and the XENON collaboration which will be described in more detail in the next chapter.

The challenge of this method is the very low event rate of such interactions. As a consequence, an excellent background control is necessary for the direct detection method.

1.5 WIMP matter interactions

One of the biggest arguments of further exploring the WIMPs hypothesis is the fact that it is testable. Because it is a hypothetical particle, it is unknown how it will interact with ordinary matter. Within the scope of this thesis we assume that WIMPs scatter elastically from nuclei (due to the kinematics the electron WIMPs scattering is strongly suppressed). The total number of events can be calculated classically by the following formula:

$$R = \frac{N_A}{A_T}\sigma\phi = \frac{N_A}{A_T}\sigma n\langle v\rangle = \frac{N_A}{A_T}\frac{\rho}{m_\chi}\sigma\langle v\rangle \tag{1.3}$$

Where N_A denotes Avogadro's number, σ is the WIMP nucleus cross-section ϕ the flux and A_T the atomic mass number of the target. $\langle v\rangle$ is the average of the relative velocity of the WIMP with respect to the target. This average follows from a Maxwell-Boltzmann that arises from the standard halo model [12]. Given by:

$$f(\vec{v}) = \left(\frac{m_\chi}{2\pi k_b T}\right)^{3/2} exp\left(\frac{-m_\chi|\vec{v}|^2}{2k_b T}\right) \tag{1.4}$$

[2]In principle, an experiment could record all three signals, but such experiments do not exist.

Also, the cross-section σ does depend on the dark matter velocity momentum transfer and therefore on the recoil energy E_R. These dependencies convert equation 1.3 to:

$$\frac{dR}{dE_R} = \frac{N_A}{A_T}\frac{\rho_0}{m_\chi}\int v \cdot f(v)\frac{d\sigma}{dE_R}(E_R, v)dv \tag{1.5}$$

Which can be simplified by using the distribution from equation 1.4 and integrate from 0 to an infinite escape velocity [3]. This yields:

$$\frac{dR}{dE_R} = \frac{R_0}{E_0 r}\exp\left(\frac{-E_R}{E_0 r}\right) \tag{1.6}$$

where R_0 is given by equation 1.3 with $\langle v\rangle = \frac{2}{\sqrt{\pi}}v_0$ and $E_0 = \frac{1}{2}m_\chi v_0^2$. r is a kinematic factor that sets a limits on the energy that is transferred in a WIMP nucleus collision.

$$r = \frac{4m_\chi m_N}{(m_\chi + m_N)^2} \tag{1.7}$$

Where m_N is the mass of the nucleus. In order to compare experiments with different target materials, the more relevant quantity is the WIMP nucleon cross-section. This WIMP nucleon cross-section is often split into a part that describes the coupling to spin of the nucleus (spin-dependant) and a cross-section that represents the coherent coupling of the nucleons (protons and neutrons) to the WIMP (spin-independent).

In case of the spin-dependant(SD) cross-section the differential cross-section is:

$$\frac{d\sigma_{SD}}{dq^2} = \frac{8G_F^2}{\pi v^2}\Lambda^2 J(J+1) \tag{1.8}$$

where $\Lambda = \frac{1}{J}(a_p\langle s_p\rangle + a_n\langle s_n\rangle)$. It should be noticed that an even number of protons will yield a $\langle s_p\rangle = 0$ same holds for neutrons. So only isotopes with an odd number of protons or an odd number of neutrons can undergo spin dependant couplings. Equation 1.8 can be integrated over momentum transfer q^2 this yields the total spin-dependent cross-section:

$$\sigma_{SD}(\chi + N) = \frac{32}{\pi}G_F^2\mu^2\Lambda^2 J(J+1) \tag{1.9}$$

This is possible under the assumption that the cross-section is isotropic. μ is the reduced mass of the WIMP nucleus system. To compare experiments with different targets, the quantity that is used is the WIMP-nucleon cross-section given by:

$$\sigma_{SD}(\chi + p, n) = \frac{3}{4}\frac{\mu_{p,n}^2}{\mu^2}\frac{J}{J+1}\frac{1}{\langle s_{p,n}\rangle}\sigma_{SD}(\chi + N) \tag{1.10}$$

To derive this quantity it is assumed that the WIMP only interacts with protons, while zero for neutrons, or the other way around. $\mu_{p,n}$ the reduced mass of the WIMP proton or neutron system.

The Spin independent case is different in the sense that one assumes that the WIMP the same to the protons as to the neutron and that the WIMP scatters coherently on the nucleus. When making this assumption, the differential cross-section follows directly from fermi's golden rule [12].

$$\frac{d\sigma_{SI}}{dq^2} = \frac{1}{\pi v^2}A^2 f_p^2 \tag{1.11}$$

[3] Escape velocity is 544 km/s, but this is ignored in the calculation because it would cut off only 0.66% of the distribution [6]

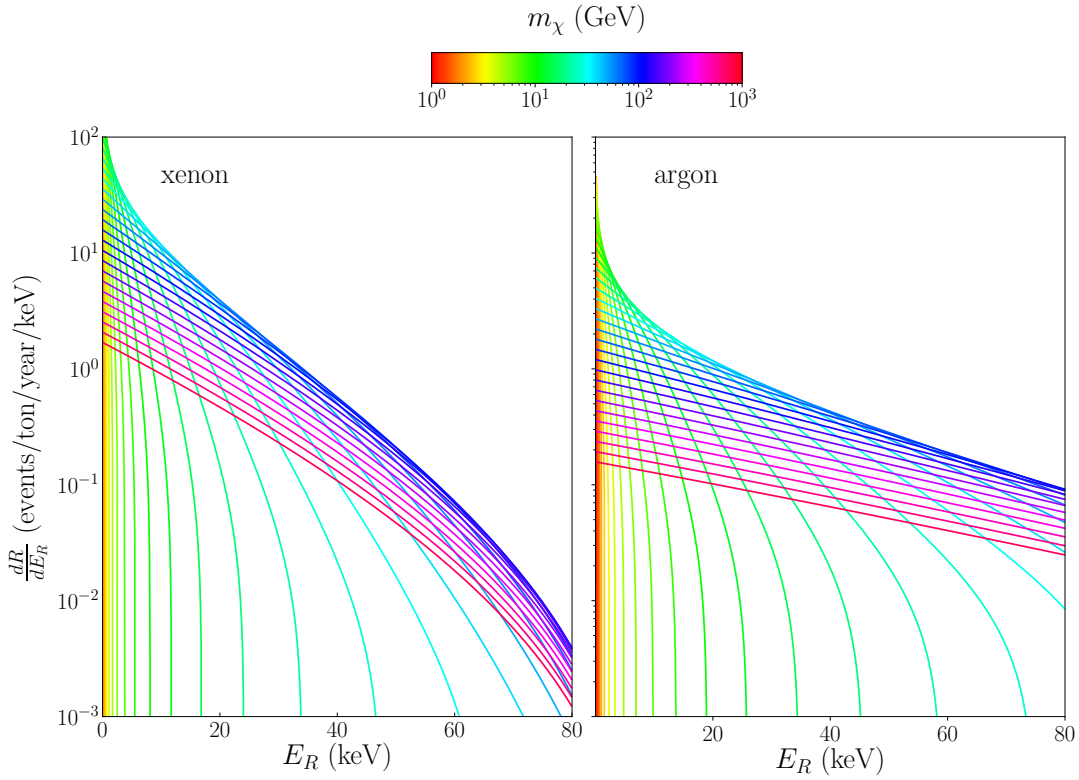

Figure 1.7 – Expected recoil energy spectra for various WIMP masses, for xenon (left) and argon (right), targets with $\sigma = 1.0 \times 10^{-45} cm^2$ as the spin-dependent cross-section. The curves take the nuclear form factor into account. For high WIMP mass, the rate is lower due to the lower number density. The calculations are based on derivations found in [12]. (From [6] [7])

Where $f_{p,n}$ is the coupling strength between the proton or neutron to the WIMP. From this it follows that the total cross-section is:

$$\sigma_{SI}(\chi + N) = \frac{4}{\pi} m_p^2 f_p^2 \frac{\mu^2 A^2}{m_p} = \sigma_{SI}(\chi + p) \frac{\mu^2 A^2}{m_p} \tag{1.12}$$

Where the WIMP-nucleon is defined as $\sigma_{SI}(\chi + p) = \frac{4}{\pi} m_p^2 f_p^2$

In general, the SD cross-section is dominant for targets with lower atomic mass ($A \lesssim 40$) for higher atomic mass the SI term becomes dominant due to the A^2 dependency (see figure 1.7)[12].

Experimental results of dark matter experiments are usually presented in a WIMP mass cross-section exclusion plot [4]. Because experiments do not detect a WIMP interaction, one can exclude a region of the parameter space (WIMP mass x WIMP cross-section). An example of such exclusion limits are shown in figure 1.8 where the lines are the limits and the region above the line is excluded.

[4] Unless an experiment does detect DM than it will show something else.

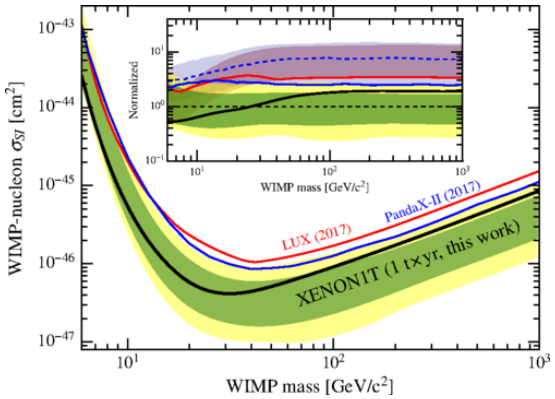

(a) XENON1T 90% C.L. upper limit on the spin independent(SI) WIMP-neutron cross section from a 1 tonne-year exposure. The range of expected sensitivity is indicated by the green (1σ) and yellow (2σ) bands.[29]

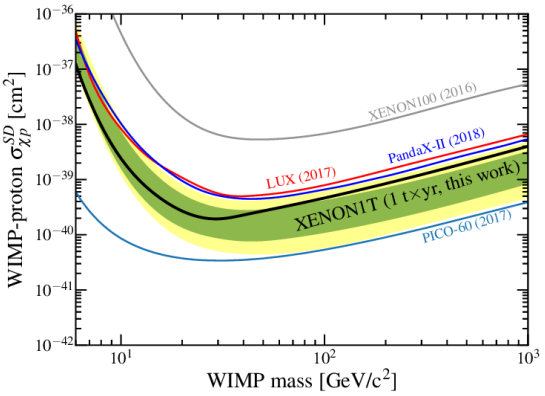

(b) XENON1T 90% C.L. upper limit on the spin dependent(SD) WIMP-neutron cross section from a 1 tonne-year exposure. The range of expected sensitivity is indicated by the green (1σ) and yellow (2σ) bands [30].

Figure 1.8

Chapter 2

The XENON Dark Matter research project

As seen in the previous chapter, there is a lot of new physics to be discovered through the detection (or no detection) of dark matter. The XENON collaboration aims to directly detect WIMPs by utilizing a time projection chamber filled with a liquid xenon target. The XENON1T experiment holds the current record on the lowest WIMP-nucleon spin-independent cross-section. These results are shown in figure 1.8. At the moment of writing the successor of XENON1T, XENONnT is constructed in Hall B of the Gran Sasso National Laboratory. This will be one of the most competitive experiments to detect dark matter by investigating a new region of the mass - cross-section parameter space.

In this chapter, the XENON experiment will be described in more detail.This will be done by explaining the detection principles of such an experiment, the basic design, and the importance of backgrounds.

Furthermore, there is a section on (future) experiments that are able to investigate different parts of the parameter space.

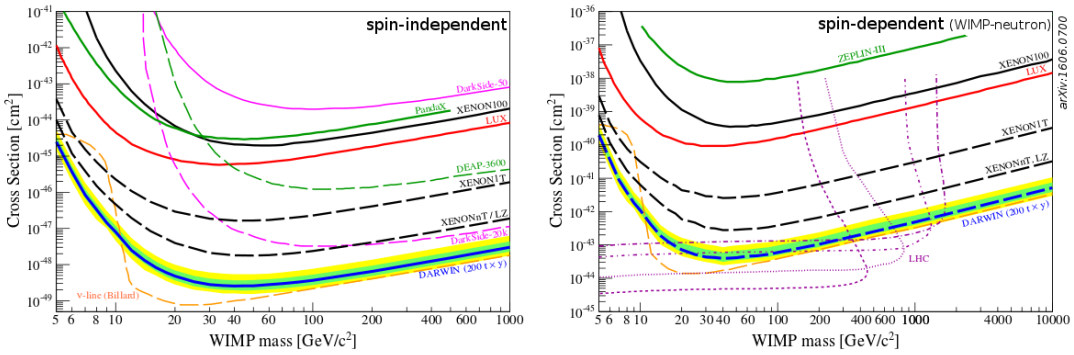

Figure 2.1 – The WIMP mass-Cross Section exclusion plots for both SD and SI couplings. With the projected sensitivities of XENONnT LZ and DARWIN. The dashed line from XENON1T is also projected data since the plot was made before the results were published. The colour band around the DARWIN line are the 1 σ yellow and 2σ regions. Neutrino floor is the dashed orange line [31]

2.1 Detection principle

If a particle scatters of a xenon atom in the TPC, two different signals can be measured one due to scintillation that is called the S1 signal and the other due to ionization that is called the S2 signal. See figure 2.2 for a schematic view of this process. If a WIMP scatters of a xenon atom, it transfers some energy to either the xenon electrons or to the xenon nucleus[1]. Because of the recoil of the xenon, a short excitation and ionization can be expected. This molecular excitation of xenon is very short-lived (∼ns) and will fall back to its ground state by emitting scintillation light (S1). [2] Besides an excitation, the atom can also be ionized due to the recoil. Because of an electric field in the TPC, the freed electrons from the ionization are pulled up to the gas-liquid interface. At the interface, a stronger electric field is applied to pull the electrons out of the liquid, by doing that they will emit a second scintillation flash called S2. A typical, extracted electron will generate O(100) scintillation photons, so much stronger signal than the S1. Both signals are in the form of UV light (∼178nm) collected by the arrays of photo-multiplier tubes (PMT) on the top and the bottom of the TPC. Having two different signals allows one to deduce valuable information about the interaction. First, it is possible to determine the 3D position of the interactions. The xy-position is determined from the hit pattern of the S2 signal in the different PMTs (see the colour scale op the PMT in figure 2.2). Because there is a difference in arrival time of the S1 and S2 signals ($\sim 100\mu$s), the z position of the scatter can be determined (hence time projection). Furthermore, the ratio of the two signals can provide information on the type of interaction. When a particle scatters off the electrons of the nucleus (electronic recoil) the ratio S2/S1 is much bigger than when a particle interacts with the xenon nucleus (nuclear recoil). Lastly, it is possible to identify particles that undergo multiple interactions. Such a signal will have multiple S2 signals at different arrival times. This information is valuable because it is implausible that a WIMP scatters more than once in the detector and therefore, events with multiple interactions will be regarded as backgrounds.

2.2 Experimental design

The Experiment has a shell-like structure that is composed of two sections. The first section has the task of shielding the detector for background signals like cosmic rays and other non-WIMP particles that can cause a background signal. The other section is the detector with the target xenon in it.

The shielding is done by placing the experiment underground and in a water tank. The overhead rock stops most of the cosmic rays (Muon flux is reduced to $3.41 \pm 0.01 \cdot 10^{-4} \mathrm{m}^{-2} \cdot \mathrm{s}^{-1}$ what is four orders of magnitude smaller than the sea level flux [32]). While the water tank prevents other background particles and the residual cosmic rays from entering the detector. The water tank also acts as a Cherenkov detector see section 2.3.3 from more details.

The inner part of the experiment consists of a cryostat vessel with a TPC inside and supporting systems keep the liquid xenon to cryogenic temperatures. The vessel is made of a double-walled cylindrical stainless-steel cryostat. The cooling system is placed outside the water tank and is connected to the cryostat by double-walled cryogenic pipe. This system makes sure that the xenon stays at an operating temperature of $T_O = -96°\mathrm{C}$ [33].

As discussed in section 2.1, the TPC should be able to detect both the S1 and the S2 signal. To do this, the two main components of the TPC are the parts that produce an electric

[1] As mentioned in chapter 1 WIMP electron scatter signal is strongly suppressed

[2] is not entirely accurate, ionization will also produce some light.

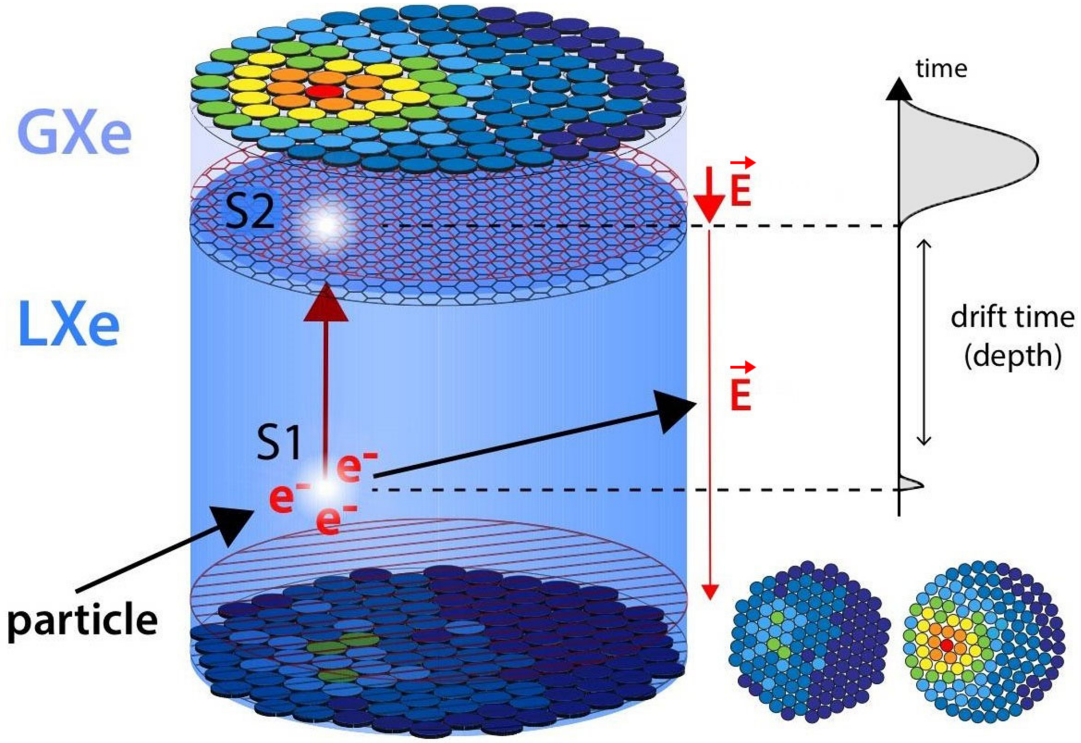

Figure 2.2 – A schematic picture od an interaction in the XENON1(n)T TPC. An incoming particle interacts with the liquid xenon (LXe) with a Xenon nucleus or the electrons and deposits some energy. This energy causes excitation and ionization of the xenon atom. The excitation is short-lived, and when it falls back, it emits a light signal that is detected by the photomultiplier tube (PMT) arrays at the top and the bottom of the TPC. This is called an S1 signal. Because the atom is also ionized, some electrons are freed. These free electrons are pulled to the gas-liquid interface where they emit a second scintillation signal (S2) that is also detected by the PMT arrays. The xy position of the interaction can be determined using the S2 signal and the z position calculated by the time delay between the signals.

field within the TPC and the system that collect the different signals. The electric field is produced by a cathode at the bottom and the anode at the top. To make sure the electric field is homogeneous, a field cage is used comprised of (40 for XENON1T) equidistant electrodes, made from copper rings. The XENON experiment studies the reactions by looking for light-signals (see section 2.1). Arrays of photomultiplier tubes (PMTs) are placed above the anode and below the cathode to collect these light signals (127 PMTs above and 121 PMTs below in XENON1T). A schematic picture of the TPCs is shown in figure 2.3.

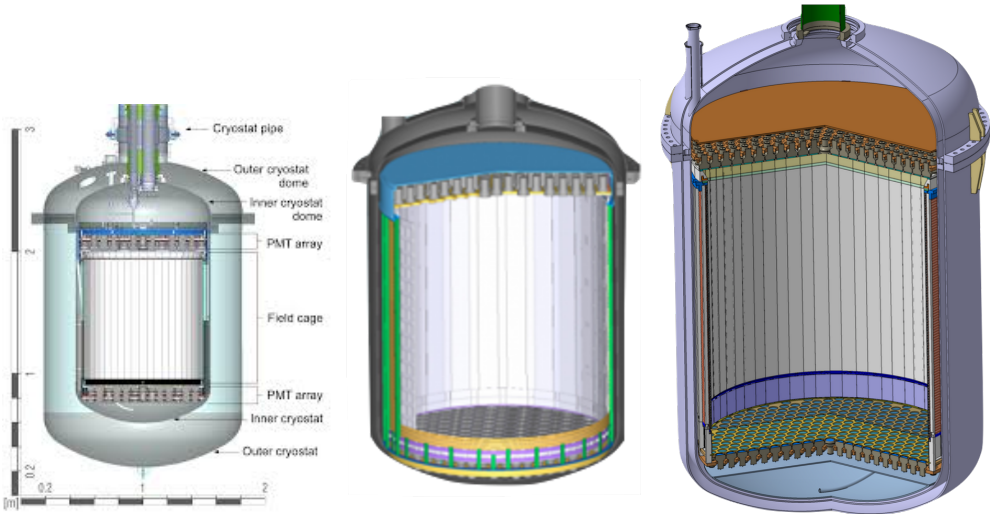

(a) XENON1T detector **(b)** XENONnT **(c)** DARWIN

Figure 2.3 – Illustrations of the different detectors not to scale. The XENON1T detector contains 3.2 tons of liquid Xenon, with 2 tons fiducial volume and has a linear diameter of 0.96m. The XENONnT detector will contain 8.4t LXe, with 5.9 tons fiducial volume and will have a linear diameter of 1.4m. The DARWIN detector will contain 50 tons of LXe, with 40 tons fiducial volume and will have a linear diameter greater than 2.5m.

2.2.1 Xenon properties

Xenon makes, because it has some very attractive characteristics, an excellent target material. As seen in section 1.5, one of the biggest advantages is its atomic mass and high atomic number: these contribute to a relatively high WIMP-nucleus cross-section.
Another feature is a property called *self-shielding*, and that is utilized to control backgrounds. Due to the short path length of relevant backgrounds like gamma-rays and neutrons in xenon (figure 2.6), most of the backgrounds that originate from outside the detector will have an interaction in the outer edge detector. By not taking into account the interactions that happen in the outer part of the active volume, the *self-shielding* is utilized to significantly reduce the background rates. The remaining inner volume is called the fiducial volume. And thanks to *self-shielding*, this fiducial volume has a very low background.
As explained in section 2.1, it is of vital importance that scintillation light can travel through the xenon. Because scintillation light in LXe (with impurities) has an attenuation length of ¿ 10m (much larger than the detector dimensions), this requirement is met[33]. Additionally, xenon is also a good scintillator by itself (compared with organic scintillator), which contributes to a lower energy threshold [29].

	Full	Reference
Electronic recoils (ER)	(62 ± 8)	$(0.26^{+0.11}_{-0.07})$
Radiogenic neutrons (n)	0.05 ± 0.01	0.02
CNNS (ν)	0.02	0.01
Accidental coincidences	0.22 ± 0.01	0.06
Wall leakage (wall)	0.52 ± 0.3	0.01
Anomalous (anom)	$0.10^{+0.10}_{-0.07}$	0.01 ± 0.01
Total background	63 ± 8	$0.36^{+0.11}_{-0.07}$
$50GeV/c, 10^{-46}cm^2$ WIMP	1.66 ± 0.01	0.82 ± 0.06

Table 2.1 – Listed are the six main backgrounds in the ROI of XENON1T (Full). The reference column lists the values after an S2/S1 cut.[34]

2.3 Backgrounds

Since the WIMP flux is constant, the only thing to improve the sensitivity is to build either a larger detector and reducing the background. It is of great importance to minimise the backgrounds to extremely low levels; hence the term low background experiments. In general, there are two types of backgrounds those who leave an electronic recoil (ER) and those that induce a nuclear recoil(NR). An important note is that the classification ER and NR is made based on the underlying process. In the analysis, signals are disgusted by an S2/S2 cut; however, some ER *leak* into the NR region. Table 2.1 shows the backgrounds in the fiducial volume.

2.3.1 Electronic recoil backgrounds (ER)

When a particle interacts with the electrons of the xenon atoms, it gives a signal that is called an electronic recoil. Beta decays within the detector volume produce a signal similar to such electronic recoils and therefore are also considered electronic recoils.

Backgrounds from detector components

The backgrounds that are most relevant for this work are gamma-rays induced by detector materials. These detector parts produce backgrounds since they contain radioactive isotopes from the ^{238}U and ^{232}Th chains as well as neutron activated isotopes like ^{60}Co. Most of these isotopes undergo an α or β decay. In most of these decays, the daughter nucleus is left in an excited state and falls back to the ground state by emitting one or more gamma-rays with energies from tens of keV up to 2.6MeV [35]. The α and β particles do not pose a significant background because they are not able to reach the active part of the detector due to their short range. Most gamma-ray will also be stopped in the outer parts of the detector (see figures 2.6 and 2.5); they are easily filtered out by fiducialization. However, a small fraction of the gamma-rays will penetrate into the active volume and interact (see figure 2.4), leaving a signal that is in the WIMP region of interest (recoil energy $<$ 250keV). For XENON1T the total rate of background events from detector materials in the (1,12) keV energy range is $(7.3 \pm 0.7) \cdot 10^{-6}(kg \cdot day \cdot keV)^{-1}$, corresponding to $(30 \pm 3)/y$ in 1 t FV [36]. In larger detectors like DARWIN this rate is expected to be $\sim 19 events/y$ in for an energy range of (2,30)keV [37]. In future experiments, the relative contribution of gamma-ray backgrounds will become larger since other backgrounds will be controlled even better [31].

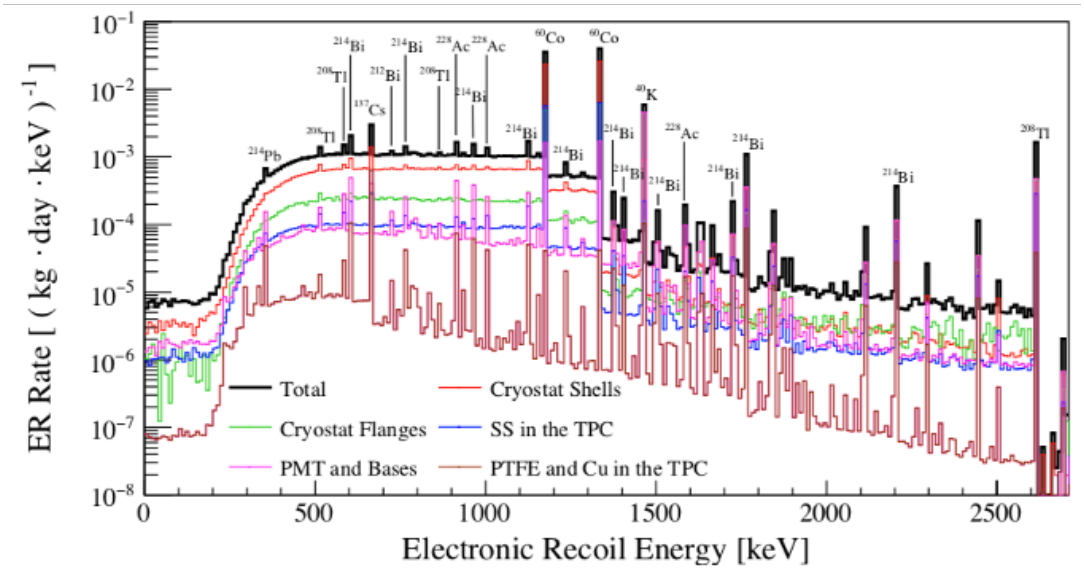

Figure 2.4 – The simulated energy spectrum of XENON1T in 1 t FV of the total ER background from the detector materials (black), and the separate contributions from the various components (colors). [36]

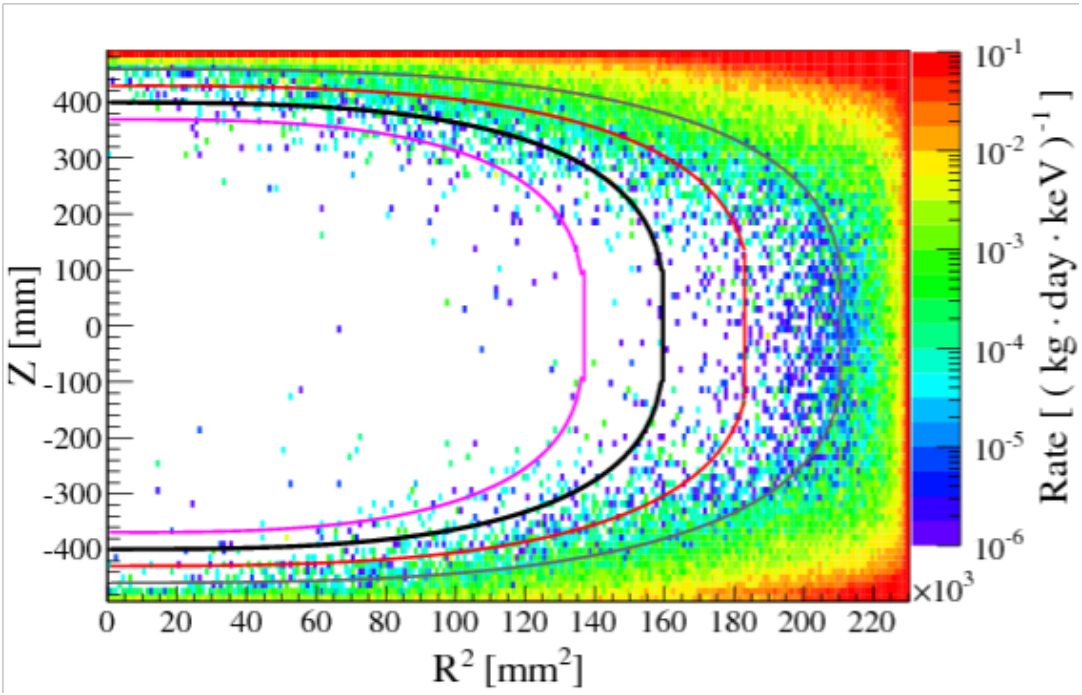

Figure 2.5 – Simulated spatial distribution of the ER background events in XENON1T from the detector materials inside the active LXe volume, in the (1, 12) keV energy range. The thick black line indicates the reference 1 t super-ellipsoid fiducial volume. With the purple, red and brown lines, we indicate the FVs corresponding to 800 kg, 1250 kg and 1530 kg, respectively. [36]

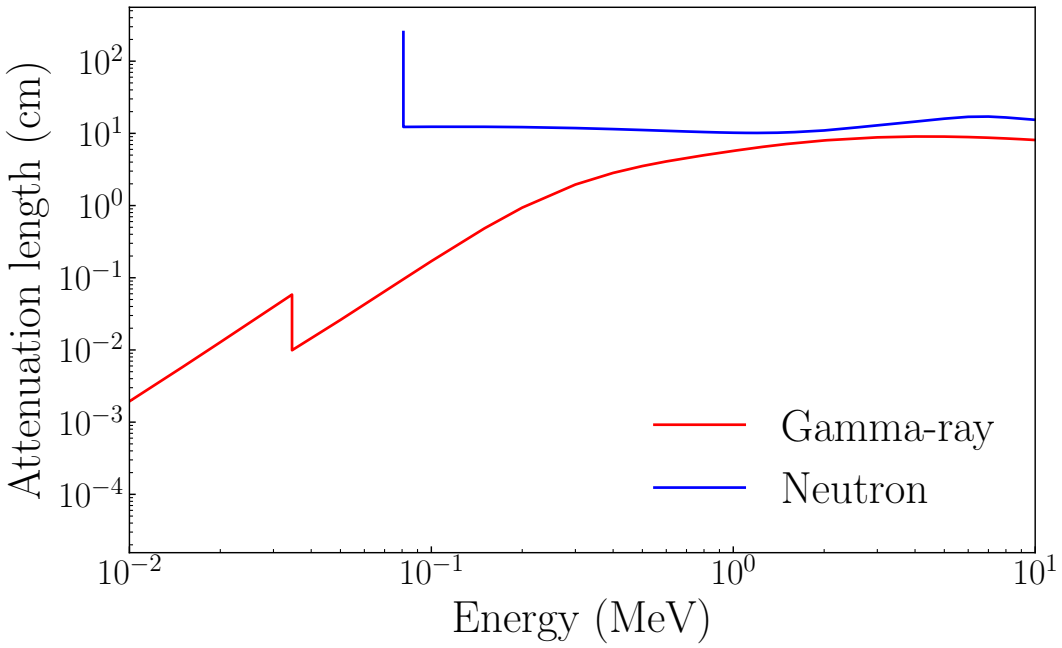

Figure 2.6 – Attenuation length of Gamma-rays (red) and neutrons (blue) in LXe of 3g/cm3. Neutron cutoff is not physical, but the data is not sufficient.[40] (From [6] [7])

Intrinsic backgrounds

More complex are the backgrounds that arise from internal radioactive decays. The most important one are the decay products of ^{222}Rn. Because of the relatively long lifetime(3.8 d [38]) of radon emitted by the detector material, it will disperse homogeneously through the detector. This is the most dominant background in the detector with an activity of 10μBq/Kg
Similarly, there are contaminations in the xenon [3] of which ^{85}Kr is the most important. Both contaminations (Radon and Krypton) can be partially filtered out of the xenon. But the radioactive isotope ^{136}Xe will always remain in the xenon since it is hard to filter out [39]. However, the beta-decay of ^{136}Xe has a relatively high q-value; therefore, it does not form a background for DM searches. But it does form a significant background for other studies that are done with the XENON detector.

External backgrounds

Besides backgrounds from the detector materials and target, external backgrounds like solar neutrinos (pp) and cosmic muons also leave an ER signal. Where the distinction must be made that muons are easily recognised in the data, whereas electron neutrino scatters are hard to identify.

2.3.2 Nuclear recoil backgrounds(NR)

The previous background all produce an electronic recoil like signal and therefore are distinguishable from expected WIMP interactions that leave a nuclear recoil. However, there are backgrounds that produce signals similar to the expected WIMP-signal, and therefore are harder to identify as backgrounds. These backgrounds are produced by particles interacting with the xenon nuclei. Most of these background signals are neutron-

[3] These contaminations are in the xenon before it is inserted in the detector.

induced [4]. These neutrons originate from detector materials that contain a tiny amount of ^{238}U and ^{232}Th and from cosmic rays. Since the lab is built underground, these cosmic rays are very rare; however, a small fraction of muons manage to traverse the 2300 m of rock $(3.31 \pm 0.03) \cdot 10^{-8} \mathrm{cm}^{-2}\mathrm{s}^{-1}$ [33]). When these muons interact with the rock (or other outer parts of the experiment), they can produce a shower of particles. These showers can contain some neutrons that are able to cause a signal that is very similar to the expected WIMP signal. To prevent this, the detector is placed in a water tank. This water tank has a twofold functionality. One it provides shielding from neutrons, and it acts as a Cherenkov detector. Besides direct effects in the form of showers, muons also activate detector materials. Those activated/radioactive materials emit background particles that are much harder to identify as background because they are time delayed.
All these backgrounds can be controlled to have acceptable levels [5]. However, if detectors become more sensitive coherent neutrino scatting is expected to occur. These signals will be impossible to control, since the detector can not be effectively shielded from neutrinos and they leave a signal that is indistinguishable from expected wimp signals. This background imposes a bound on the parameter space that can be studied by such detectors. This limit is often referred to as the neutrino floor. See the dashed orange line in figure 2.1 [6].

2.3.3 Background Control

Minimising backgrounds is done (if possible) by combining three methods. These methods are based on preventing backgrounds, knowing when a background event occurs and filter events out based on event characteristics.
The first one is to prevent background events. This is done by, placing the experiment underground and in a water tank, filtering contaminations like ^{85}Kr out of the xenon, cleaning the detector parts to remove radioactive isotopes from surfaces, selecting materials that are in contact with xenon for low Rn emanations [41] and screening detector materials for low activity.
The second is to know when a background signal could be generated and veto them out. The water tank not only shields the detector but also recognises entering particles such as muons. The light produced by the muons when penetrating the water is detected by PMTs inside the water tank. Events inside the TPC which happen time coincident with the muon detector are now vetoed from the DM analysis since they are most likely induced by muons. The XENONnT will also be equipped with a neutron veto. The n-veto will identify neutrons from the detector materials. This is done by identifying neutrons which scatter inside the TPC and then leave the detector. Outside the TPC they are trapped and identified by the n-veto [42].
Lastly, it is possible to cut out events based on their characteristics. Two main strategies are employed to do this. One is by choosing an active volume of your detector this is called fiducialization. By doing this, one can optimise the signal to noise ratio. Another characteristic to filer out background events is by looking at the S1 S2 signals of single events. By investigating the rations between these two values, it is possible to identify electronic recoils and high energy depositions and filter them out and by rejecting events with multiple S2 signals.
By combining all these measures, XENON1T achieved an ultra-low background of $82^{+5}_{-3}(sys) \pm 3(stat) events/(t \times yr \times keV_{ee})$ electronic recoils and $1.4 \pm 0.6 events/(t \times$

[4] At the moment all NR are neutron-induced, but it is expected that neutrinos can also leave an NR signal.

[5] controlled relatively good, in general lower background is always better

[6] If in far future detectors it would be possible to measure the direction of the incoming neutrino it would be possible to filter them out since they come from the sun.

$yr \times keV_{nr}$) nuclear recoils in the WIMP region of interest [29].

2.4 Future detectors

At the time of writing (2020), XENONnT is being assembled at LNGS. However, plans for a future liquid xenon dark matter experiment are made. This DARk matter WIMp search with liquid xenoN (DARWIN) is planned to be a dual-phase liquid xenon detector with an active volume of 40 tons [31]. Its goals will depend on other major experiments that will have been conducted before DARWIN will be built. In the case that experiments like XENONnT and LZ [28] do not find evidence for a dark matter interaction DARWIN would aim to discover dark matter or will be used to lower the detection limit even further right towards the neutrino floor. Should dark matter particles be discovered by other experiments DARWIN will be used to do a precision measurement on the nuclear recoil spectra and provide better statistics to constrain the mass of the particle. For such large detectors, a better understanding of the backgrounds is necessary because of rare processes like a neutron interacting in the fiducial volume become more prone to happen. Therefore it is essential to develop software that can be used to understand and study these rare background events even better.

Chapter 3

Photon transport

Gamma-rays from detector materials form a relevant background in LXe experiments. To be able to control and accurately describe such backgrounds, one needs a thorough understanding of the microphysics that form these backgrounds. In this chapter, the production mechanisms will be explained as well as the possible interaction mechanisms. Besides that, the propagation of gamma-rays will be explained using the Beer-Lambert law of attenuation.

3.1 Production mechanisms

To have a good understanding of gamma-rays, it is crucial to know where they originate from. There are multiple processes where a gamma-ray can be produced. The most important is a through a beta decay. This process will be explained in more detail, while other processes that are less relevant will be explained more briefly.

The most important production mechanisms of a gamma-rays is through a beta decay. In this process, the parent nucleus undergoes a beta decay, but the daughter nucleus is produced in an excited state. This excited nucleus than falls back to its ground state and thereby emitting (multiple) gamma-ray(s). The two steps of this process have an interesting influence on the characteristics. In most (relevant for LXe detectors[1]) cases is the beta-decay a relatively slow process with lifetimes of multiple days, whereas the lifetime of the exited daughter nucleus is often on the order of picoseconds. Therefore, the characteristic lifetime of the (gamma-ray)decay appears to be that of the parents beta decay. In contrast, the energy of the gamma-ray only depends on the energy levels of the daughter nucleus. These levels are in general much further apart than the electron energy levels, because they originate from the strong nuclear force [35]. An example of such a gamma-ray production is the decay of 60Co (which is neutron activated).

$$\begin{aligned} {}^{60}\mathrm{Co} &\rightarrow {}^{60}\mathrm{Ni}^{*} + e^{-} + \bar{\nu}_e \\ {}^{60}\mathrm{Ni}^{*} &\rightarrow {}^{60}\mathrm{Ni} + \gamma(1.17\,\mathrm{MeV}) + \gamma(1.33\,\mathrm{MeV}) \end{aligned} \tag{3.1}$$

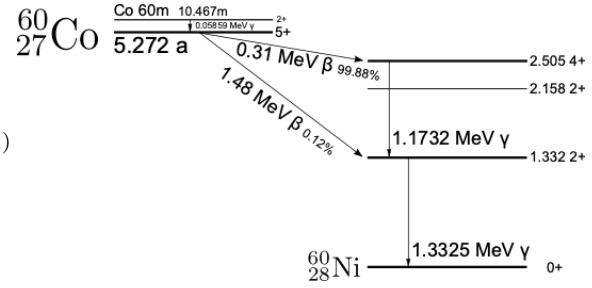

[1]Decays with short lifetime will not survive long unless another isotope with long decay time produces them.

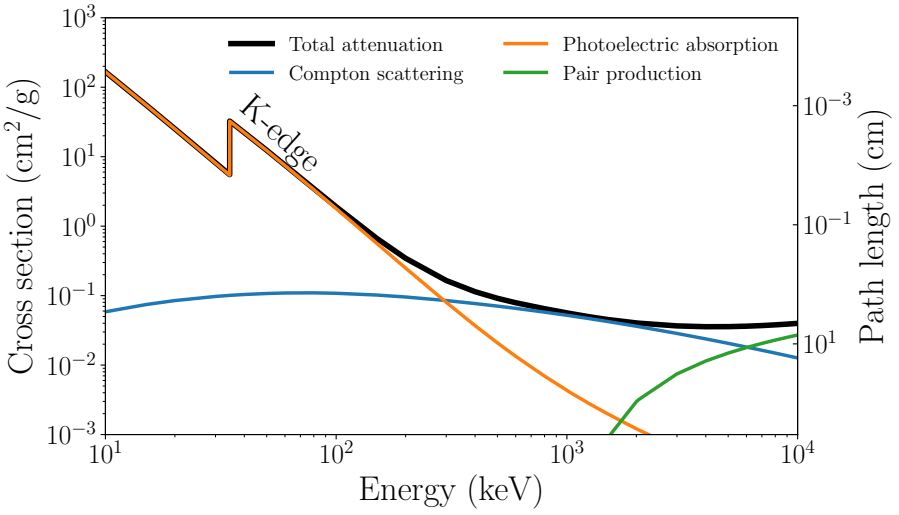

Figure 3.2 – Gamma-rays cross-sections in LXe as a function of photon energy. The total cross-section is shown by the black line, and the coloured lines show the cross-sections of the different processes.(From [6] [7])

There are other gamma-ray sources, but they are of less importance in the study of backgrounds events in LXe detectors. In one mechanism the gamma-ray is produced by the annihilation of positrons that originate from β^+ decay with electrons. In this process, both gamma-rays have an energy of 511 keV [2] [35].Because they only appear in combination with other events, they are easily filtered out. Another production mechanism is the alpha-decay equivalent of the beta-decay explained above, but where the initial decay is an alpha[35]. The gamma-rays produced by such decays have in general energies far above the ROI. Furthermore, fast electrons can also produce radiation through Bremsstrahlung and Synchrotron [35] which are not relevant to these experiments.

3.2 Interaction mechanisms

Gamma rays can have three interactions with matter, namely photoelectric absorption, Compton scattering, and pair production. Besides those interactions, it is possible to have a coherent scattering. In this section, all processes will be explained.

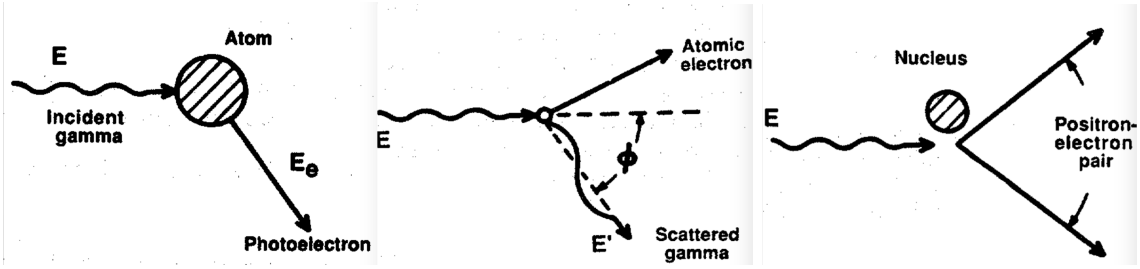

(a) Photo-electric absorption **(b)** Compton-scattering **(c)** Pair-production

Figure 3.1 – A schematic representation of the three main interaction processes

[2] can be more to conserve momentum, but most of the time the position is sufficiently slowed down before anhilating

3.2.1 Photoelectric absorption

The first possible interaction is photoelectric absorption. In this case, the gamma ray interacts with the bound electrons of an atom. In this process, the gamma-ray is absorbed[43]. The energy that is deposit is used to liberate an electron from its bound shell, and the rest is transferred to the freed electron in the form of kinetic energy.[3]

$$E_{e^-} = E_\gamma - E_b \tag{3.2}$$

Where E_{e^-} is the energy of the freed electron, E_γ is the energy of the indecent photon, and E_b is the binding energy of the shell where the electron is freed from.

After the electron is liberated, the vacancy is filled up with an electron from a higher shell and thereby emitting a cascade of characteristic X-rays. However, sometimes (12% of the time in LXe [6]) the excitation energy is emitted in the form of an Auger electron. Since both the X-rays and the Auger electrons have a very limited range (mm scale for X-rays and μm for Auger electrons [35]) compared to a typical detector resolution, it is safe to state that all the energy of the gamma-ray is deposited in a single position.

As shown in figure 3.2, for low photon energies (< 300 keV), photoabsorption is dominant. However, the interaction probability is also specific to the absorber properties like binding energy of the shells and atomic mass number. Interactions with the tightly bound electrons are more likely. Therefore, when there is sufficient energy($E_\gamma >$ binding energy K shell), most interactions happen with K electrons (86% of photons with more than 30 keV, in xenon [35]). Also, the probability is increased in a material with a high atomic mass number Z. This relation is approximated by:

$$\tau \simeq constant \times \frac{Z^n}{E_\gamma^{3.5}} \tag{3.3}$$

where τ is the photoelectric attenuation coefficient (see section 3.3) and the exponent n varies from 4 to 5 depending on the gamma-ray energy.

3.2.2 Compton scattering

Another interaction that is most relevant for the study of low energy backgrounds is the Compton effect. This effect describes a photon that scatters of a free or loosely bound electron. In this process, the photon is deflected at an angle θ and transfers some of its energy (dependant on the angle) to the electron [43]. The formula below gives the relation between the energy of the incoming and outgoing photon as a function of the scattering angle:

$$E'_\gamma = \frac{E_\gamma}{1 + \frac{E_\gamma}{m_e c^2}(1 - \cos\theta)} \tag{3.4}$$

Where E_γ is the energy of the photon before the scatter, E'_γ is the energy of the photon after the interaction, m_e is the rest mass of the electron and θ is the deflection angle of the photon. After the interaction, the photon propagates further and is able to undergo a second scatter or an absorption.

Compton scatters can deposit energies over a range due to the angle dependency (see figure 3.3). This range produces a broad spectrum of energy deposits in a detector. A typical

[3] Not completely accurate, since some of the energy is transferred to the atom as recoil energy. This must happen to oblige to momentum conservation.

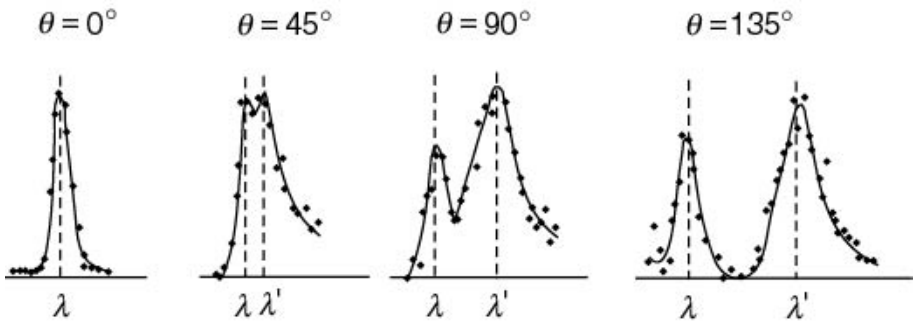

Figure 3.3 – Shift in wavelength as measured by Arthur Compton. The test setup was an x-ray beam shot at a graphite target, and the intensity as a function of wavelength is measured at different scattering angles around the target. Peaks on the left(λ) are due to coherent scatters, and the shifted (λ') are due to the Compton-effect[44]

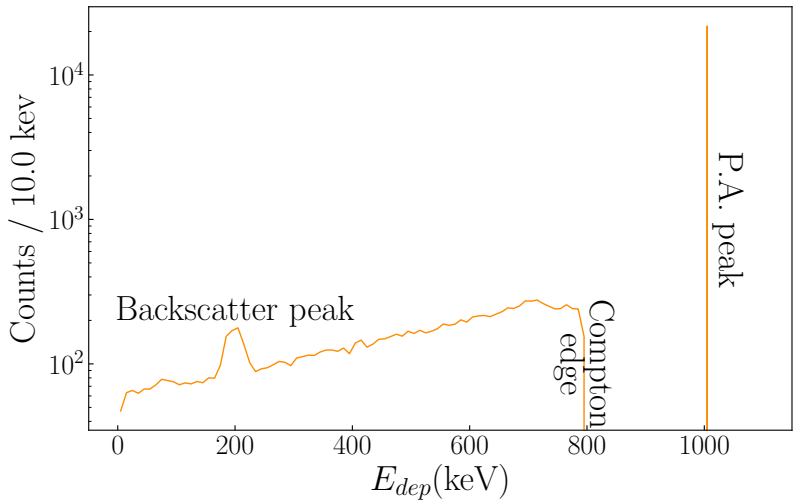

Figure 3.4 – The spectrum of energy deposits produced by a 1MeV gamma ray in a Lxe filled vessel. Spectrum is obtained using a MC simulation.(From [6] [7])

spectrum of single scatter 1MeV gamma-rays is shown in figure 3.4. These Compton spectra have two important characteristics: one is called the Compton edge and the other is the backscatter peak, The Compton edge arises from the limit on deposited energy. This maximum is found by solving equation 3.4 for a head-on collision ($\theta = 180°$) which leads to:

$$E_{\gamma,min} = \frac{m_e c^2}{\frac{m_e c^2}{E_\gamma} + 2} \tag{3.5}$$

$$E_{dep,max} = \frac{E_\gamma}{\frac{m_e c^2}{2E_\gamma} + 1} \tag{3.6}$$

Where $E_{\gamma,min}$ is the minimal energy of the photon after the interaction and $E_{dep,max}$ is the maximum energy deposition due to a Compton scatter and therefore $E_{dep,max} = E_{Comptonedge}$. The other distinct feature is the backscatter peak (at $E_{backscatter} \approx E_{\gamma,min}$), which arises from gamma-rays that have a head-on collision outside the detector after which they travel into the detector to undergo a photoelectric absorption. Compton interaction is the dominant process for $E_\gamma >> E_{binding}$. For Compton interaction the

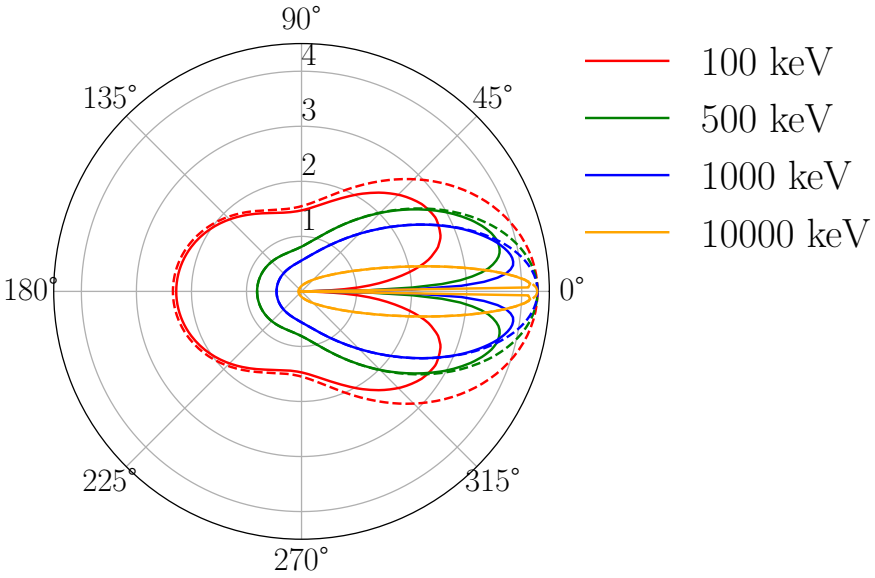

Figure 3.5 – Polar distributions of the solid angle of scattered photons as described by the KN-angular cross-section. The solid lines represent the cross-section with form factors and the dashed line without form factors. Note the inclination toward small angles for high energy gamma-rays.(From [7])

angular distribution of gamma-rays is given by the following formula:

$$\frac{d\sigma}{d\Omega} = F(\theta) \cdot \underbrace{Zr_o^2 \left(\frac{1}{1+\alpha(1-\cos\theta)} \right)^2 \left(\frac{1+\cos^2\theta}{2} \right) \left(1 + \frac{\alpha^2(1-\cos\theta)^2}{(1+\cos^2\theta)[1+\alpha(1-\cos\theta)]} \right)}_{\text{KN}} \tag{3.7}$$

Where part KN is the Klein-Nishina differential cross-section with $\alpha = E_\gamma / m_e c^2$ and r_0 [35] is the classical electron radius and $F(\theta)$ is the form factor that accounts for the binding energy of the atoms [45].

Where the polar plot is shown in figure 3.5, and it tells that high energy gamma-rays have a tendency to undergo a forward scattering.

3.2.3 Pair production

The third interaction process is pair-production. For high gamma-ray energies($>$ 1.02 MeV, twice restmass of an electron), a photon can convert into an electron-positron pair. This happens in the Coulomb field of an nucleus. The excess energy of the photon (everything above 1.02MeV) is carried away by the electron-positron pair [35]. Because the positron will be slowed down and subsequently annihilate and produce two photons, a secondary signal can be detected. The energy threshold for pair production to occur is 1.02 MeV, but in practice the probability becomes significant for gamma-rays with energies of several MeV and even becomes the dominant interaction for such a gamma-rays (see figure 3.2). As mentioned, there is no simple explanation for the interaction probability, but it is known that the interaction probability varies with the square of the absorber atomic number Z. For example, a 1.5MeV gamma-ray will have interaction probability of 20% in lead and 2% in carbon, and for a 2.0MeV this rises to 50% and 4% respectively [43]. From figure 3.2 it follows that pair production becomes dominant only for high energetic gamma-rays ($>$ 7MeV), it is of less importance when studying low energy ($<$1MeV) recoils.

3.2.4 Rayleigh scattering

Besides the incoherent interaction mentioned above, a coherent interaction between the photon and the gamma-ray is also possible. In this case, the photon scatters of the whole atom (and not with the electrons as in Compton scatters). This is called Rayleigh scattering. The behaviour of such a coherent scatter is best understood by looking at equation 3.4 and replace the electron mass by the mass of an atom, which is in the case of xenon is $2 \cdot 10^5$ times heavier than an electron [38]. It is evident that the photon will only deposit a very small amount of energy. So the energy of the photon doesn't change, and therefore it is often neglected in discussions about gamma-ray interactions. Nonetheless, the photon does change direction; therefore, it should be an interaction to take into account in a perfect simulation. However, since it is a sub-dominant process, it can often be neglected in simulation.

3.3 Gamma-ray attenuation

Besides knowing how the gamma-rays interact, it is vital to understand how photons propagate through the matter and where they might interact. To answer this question, the Beer-Lambert law is used.

$$I = I_0 e^{-\mu_l \cdot L} \tag{3.8}$$

In this equation all the information about the material is in μ_l, called the (linear) attenuation length. To include all the processes from above the three interaction probabilities are summed.

$$\mu_l = \tau(photoelectric) + \sigma(Compton) + \kappa(pair) \tag{3.9}$$

Where τ, σ, and κ are respective the probability per unit path length that the gamma-ray interacts by photoelectric, Compton, and pair-production . As mentioned in the previous section, these quantities depend not only on the atomic number but also on the density of the material. To avoid confusion, a more general quantity is often tabulated that is called the mass attenuation coefficient. This coefficient can be thought of as the effective cross-sectional area of electrons per unit mass of absorber and can be written as:

$$\mu = \frac{\mu_l}{\rho} = \frac{N_A \sigma}{A} \tag{3.10}$$

where N_A is Avagadro's number A is the atomic weight of the absorber and the cross section σ is the probability of a gamma ray interacting with a single atom. This quantity is now state-independent, but does still depend on the material. For example, the attenuation length of xenon is shown in figure 3.2.

Chapter 4

Monte Carlo simulations

Monte Carlo (MC) simulations are a common tool to investigate photon transport in matter such as liquid xenon. Since some interactions of interest have a very low probability, normal MC methods do not suffice because one needs to sample from a large set of events in order to obtain sufficient statistics on the interaction of interest. However, it is possible to extend the MC method with dedicated variance reduction techniques (VRT). Using such techniques correctly will allow increasing statistics on rare events. In this chapter, an MC method that is dedicated to simulating gamma-ray, creation, transport, and interactions in liquid xenon will be explained. Furthermore, a VRT method based on important sampling will be described.

4.1 MC method

To improve the understanding of gamma-ray induced backgrounds, a dedicated MC is developed. This method serves as the foundation for the VRT and will be used for its validation. The benefits of such a dedicated MC are that the necessary physics can be added, including form factors for Compton interactions, and the code is kept simple and accessible. Because the goal of this project was to prove the concept of the VRT, the simulation is simplified. One simplification is that the pair production mechanism is not simulated, because such interactions only happen for gamma-rays with high energy which are of less relevance for dark matter studies LXe experiments. The other simplification is made by approximating the geometry of the detector as a cylinder without any extra features.
To simulate gamma-rays through liquid xenon, three main steps need to be simulated: the creation, the transportation and the interaction.

4.1.1 Creation

For this study, the simulated gamma-rays are created uniformly on the edge of the cylinder. The first step of distributing the gamma rays over the edge of the detector is to choose if the start point lies on the side or on the top or bottom plain.

Once a side of the cylinder is picked, a creation point needs to be generated.

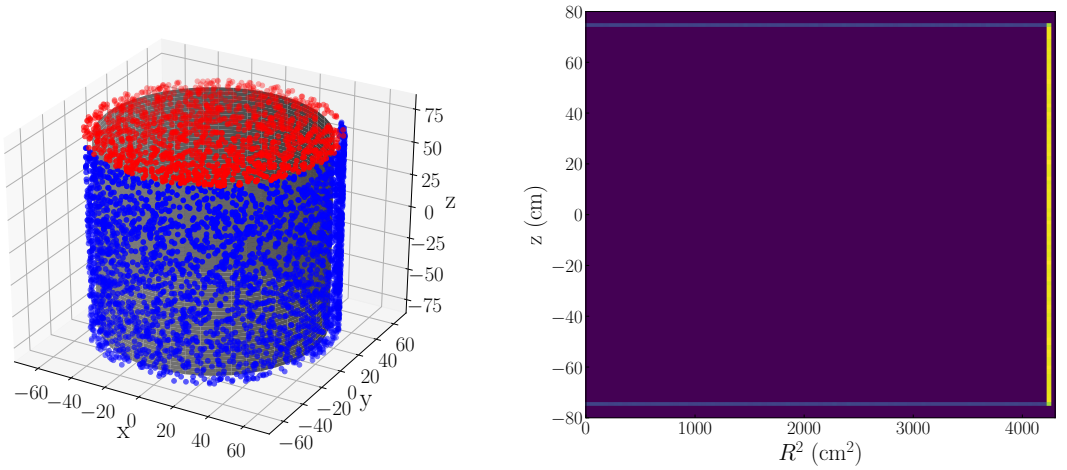

(a) Creation points on the surface of the cylinder. Colour of the points, Blue for the side and red for the top is only for graphical reasons. (From [7])

(b) 2D projection of the creation points. X-axes is represented by R^2 because this will show a uniform distribution for equal density due to the jacobian of cylindrical coordinates. Because of these coordinates systems, the side and the top/bottom are hard to compare, but one can see that the sides have a uniform distribution. (From [7])

Figure 4.1

For points on the side of the cylinder:

$$\begin{aligned}\phi &= \text{random.uniform}(0, 2\pi)\\ x &= \text{radius} \cdot \cos(\phi)\\ y &= \text{radius} \cdot \sin(\phi)\\ z &= \text{random.uniform}(-\text{height}/2, +\text{height}/2)\end{aligned}$$

For points on the top/bottom of the cylinder:

$$\begin{aligned}r &= \text{radius} \cdot \sqrt{(\text{random.uniform}(0, 1.))}\\ \phi &= \text{random.uniform}(0, 2\pi)\\ x &= r \cdot \cos(\phi)\\ y &= r \cdot \sin(\phi)\\ z &= \pm\text{height}/2\end{aligned}$$

Where radius and height are the dimensions of the cylinder and r, and ϕ are the random coordinates of the point. After the point is picked a random initial direction is assigned, by

$$\begin{aligned}\cos(\theta) &= \text{random.uniform}(-1, 1)\\ \sin(\theta) &= \sqrt{(1 - \cos(\theta)^2)}\\ \phi &= \text{random.uniform}(0, 2\pi)\end{aligned}$$

Where θ is the polar angle and ϕ is the azimuthal angle. To improve the efficiency of the MC, one could implement only forward scatters, but this would involve complex geometry, and therefore it is not implemented in this particular method.

Figure 4.1 shows the creation points of the 10^3 gamma-rays; it is clear that they are evenly distributed.

4.1.2 Transportation

Simulating the transport can be done on different levels. Most common and efficient is calculating the mean free path (attenuation length) of the photon and use that quantity to simulate an interaction point. This calculation is done in a four-step process. The first step is to calculate the attenuation length of the photon and the maximum path that the

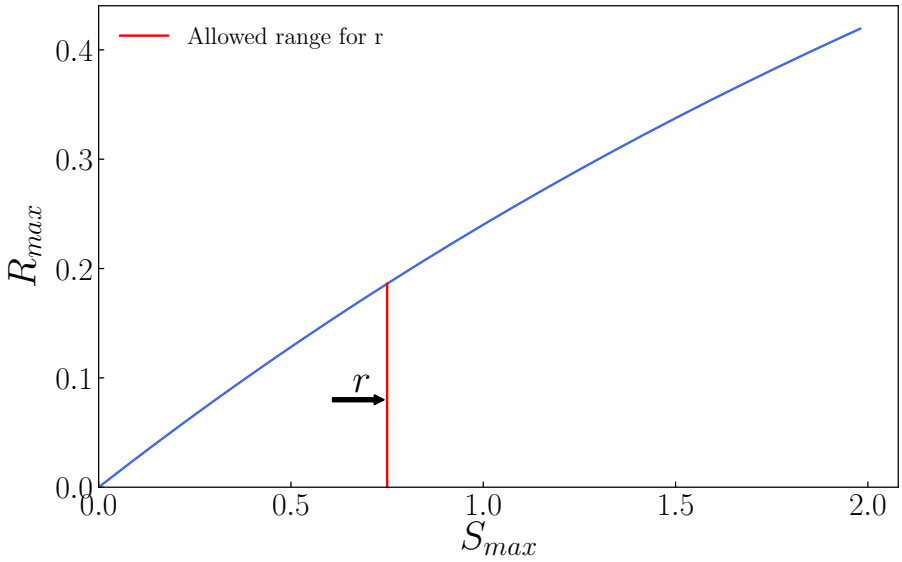

Figure 4.2 – Distribution of maximum value of ranges for propagation length in blue. Red is allowed range for a certain possible path (picked at random). The black arrow is a (random) example of a picked value within this range.

photon can travel within the xenon (s_{max}), i.e. the distance to the edge of the volume if the photon would have travelled in a straight line.

While the maximum path length is calculated with geometry, the attenuation length is not calculated but loaded from a database. The tabled value of attenuation length is the mass attenuation coefficient μ. The most common source of this value is the table of cross-sections from NIST [40].

With these two numbers (μ and s_{max}), one can set a limit on the maximum travel lengths:

$$R_{max} = 1 - e^{-s_{max} \cdot \mu \cdot \rho} \tag{4.1}$$

Where ρ is the density of liquid xenon. The next step is to use this upper limit (R_{max}) to determine the interaction point. This is done by randomly pick a number r between 0 and R_{max}. As the last step, this random value needs to be converted to the appropriate length, by:

$$L = -\log(1 - r)/\mu \cdot \rho \tag{4.2}$$

So the photon will undergo an interaction a length L away from its previous location.

4.1.3 Interaction

When the interaction point is determined, the next step is to choose the interaction process and simulate the interaction. Selecting the interaction process is done based on the relative cross-section of the Compton effect $\sigma_{Compton}$ and the Photoelectric effect $\sigma_{P.E.}$ (from NIST table [40]). This ratio is defined as:

$$\frac{\sigma_{Compton}}{\sigma_{Compton} + \sigma_{P.E.}} \tag{4.3}$$

Since pair production is not sub-dominant for the energies that are considered, the photon can either undergo a Compton scatter or can be absorbed. Choosing between the processes is done by picking a random number between 0 and 1. If this number is larger than the

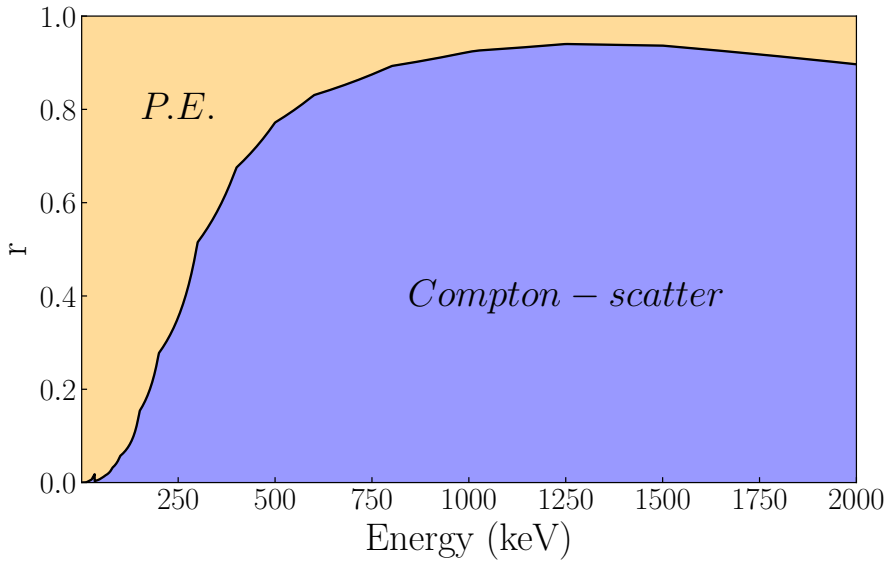

Figure 4.3 – Schematic on how the process selection is done. Random r and corresponding energy determine the interaction process. (From [7])

ratio from equation 4.3, then the photon will be absorbed. If the random number is smaller than the ratio, then the photon will experience a Compton scatter. This is illustrated in figure 4.3.

Compton scatter

When the interaction is a Compton scatter, the scattering angle needs to be simulated since this determines the energy and is necessary to simulate the photon track. To determine this angle, the NIST cross-sections are not sufficient, because they do not have an angle dependency. The Klein-Nishina angular cross-section from section 3.2.2 solves this problem. To pick a scattering angle according to the distributions predicted by the KN-formula, the CDF is calculated by integrating the formula over the possible angles. Due to the form factors, this can not be done analytically.

$$CDF(\cos\Theta) = \frac{\int_{-1}^{\cos\Theta} \frac{d\sigma}{d\cos\theta} d\cos\theta}{\int_{-1}^{1} \frac{d\sigma}{d\cos\theta} d\cos\theta} \tag{4.4}$$

Where Θ is the lower limit on the scattering angle. This CDF is shown as the blue line in figure 4.5. The CDF is than used to choose a scatter angle, and the corresponding energy deposit follows from the Compton formula from section 3.2.2. The other scatter angle ϕ does not have such an angle dependant cross-section. Therefore it can just be a random number between 0 and 2π. After all the angles and deposited energy are calculated, the gamma ray is updated with a new direction and a lowered energy ($E_{new} = E_{old} - E_{dep}$).

Photoelectric absorption

In the case of photoelectric absorption, the photon is absorbed, and a photon electron is created. Since such an electron has a mean free path length of mm [6], therefore, it suffices to simulate an energy deposit of all the photon energy on the location of the interaction and terminate the event.

4.2 Acceleration

For the simulation we consider in this research interactions in the region of interest (ROI) are extremely rare. For this reason, simulations tend to become time/CPU consuming with an extremely low efficiency. This imposes an efficiency problem that a normal MC method will simulate photons of which the majority does not interact in the region of interest. To solve this problem, alternative MC techniques have been developed to increase the efficiency of the simulation. One of these techniques that is especially useful for photon simulations is called importance sampling. For gamma-ray background estimations in a liquid xenon experiment, such as the XENON1T, the efficiency of simulating ROI events is improved using the importance sampling on the parameters that determine the ROI.

4.2.1 Importance sampling

Importance sampling (IS) is a Variance Reduction Technique that can improve statistics in a specific region of interest by overweighting the sampling in such a region, as is shown in figure 4.4. To still be able to make an accurate estimate, an adjustment needs to be made to the result. To fully understand this process, one needs to understand the principles of MC estimations.

In the case when the probability density function of a quantity is known the "estimate" is:

$$E[X] = \sum_x x \cdot f(x) \tag{4.5}$$

But if the probability distribution is not known, a way of estimating the value is to compute:

$$E_{non-biased}[X] \approx \frac{1}{n} \sum_{i=1}^{n} X_i^f \tag{4.6}$$

Where X_i^f is a random value out of the distribution of x, and n is the number of random values that are picked: this is the normal MC method. However, when the distribution has a very low probability of coming up with values in the region of interest, it can be hard to make a precise estimate on the probability of such rare events. Yet it is possible to bias the distribution to the region of interest with an alternative distribution $g(x)$. This is done by a neat trick:

$$E_{biased}[X] = \sum_x x \cdot \frac{f(x)}{g(x)} \cdot g(x) \tag{4.7}$$

The estimate $E_{biased}[X]$ can be approximated in the same manner as equation 4.6.

$$E_{biased}[X] \approx \frac{1}{n} \sum_{i=1}^{n} X_i^g \frac{f(x)}{g(x)} \tag{4.8}$$

This allows to sample from the more specific and biased distribution X_i^g, which increases the statistics in the ROI. However, one can not alter the probability function without an effect. This is accounted for in the ratio $\frac{f(x)}{g(x)}$ which is also called the importance weighting or simply the weight.

In this research, there is a clearly defined region of interest, so the biased distribution $g(x)$ is a block function over this region, as shown in figure 4.4 This results in only sampling events within the ROI.

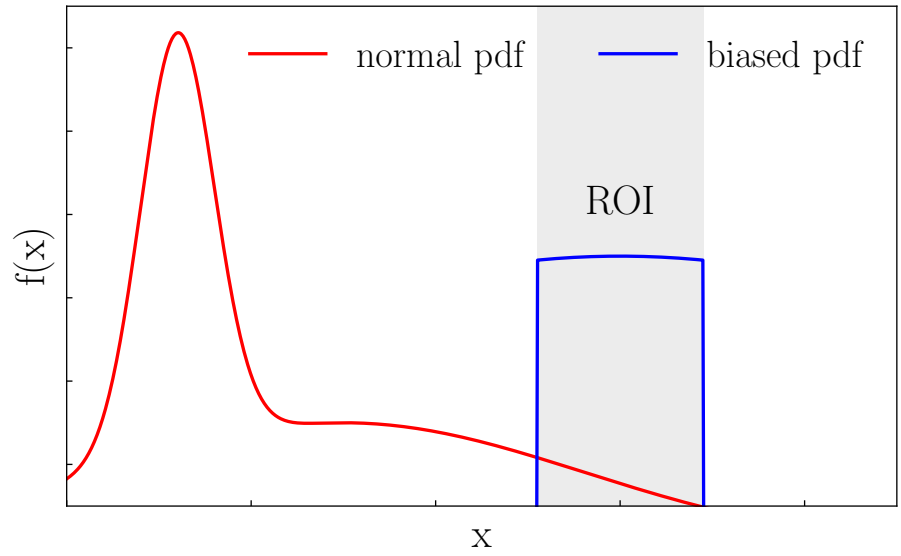

Figure 4.4 – Schematic to illustrate how a biased probability (blue line) distribution allows effective sampling of the ROI where a non-biased distribution(red line) will be inefficient in sampling the ROI. (From [7])

4.2.2 Implementation of importance sampling

To apply an IS routine to gamma-ray background estimations in a liquid xenon experiment, one needs to bias the pdf ($(f(x)$ is biased to $g(x)$) such that only events within the ROI are simulated. To do this without losing generality, weights are used to account for the biases. For each parameter that is biased, a specific weight $(f(x)/g(x))$ is assigned.

The events of interest for this particular study are the low energy single scatters in the inner part of the detector. The three parameters that make up the region of interest are the spacial location of the interaction, the number of interactions and the energy that is deposited.

The first parameter for the ROI is the spacial location of the interaction. In order to increase the number of interactions within the inner part of the detector, a transportation routine is used. This routine transports the photons from their place of creation to the volume of interest without the possibility of interacting (teleportation). By doing this, a bias is introduced which is accounted for by a weight of:

$$w_{teleport} = \exp\left(-\mu(E_\gamma) \cdot \rho |\vec{x}_1 - \vec{x}_0|\right) \tag{4.9}$$

where $\vec{x}_0$ is the point of creation and $\vec{x}_1$ is the point of the intersection with volume of interest.

The second important parameter that contains the ROI is the deposited energy. Placing a constraint on the energy deposit will have an effect on the selection of the interaction process and on the scattering angle of a Compton scatter. The constraint on the process arises when the photon has more energy than the energy cutoff $E_\gamma > E_{cutoff}$. When this happens, the photo-electric effect is turned off.

The other consequence of the energy cutoff is the limitation on scattering angles of the Compton interactions. The maximum angle for a given energy cutoff is:

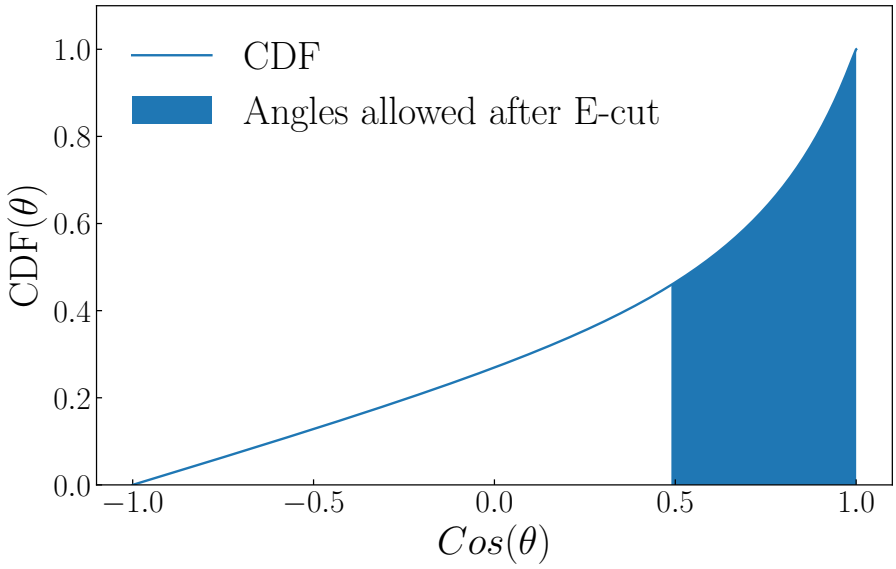

Figure 4.5 – CDF of scattering angles. The blinded region is the allowed region after energy-cutoff is made.Source code available at [7]

$$\begin{aligned} \cos(\theta)_{min} &= 1 - m_{e^-}\left(\frac{1}{E_{cutoff}} - \frac{1}{E_\gamma}\right) \\ \theta_{max} &= \cos^{-1}\left(1 - m_{e^-}\left(\frac{1}{E_{cutoff}} - \frac{1}{E_\gamma}\right)\right) \end{aligned} \tag{4.10}$$

Next, this new limit is used to blind a part of the CDF from equation 4.4 and force the photon to scatter within the allowed range of angles. Picking a scatter angle and calculate the deposited energy is done the same as in the normal MC. See figure 4.5 for this blinded CDF. Both biases that arise from the energy cutoff are accounted for by:

$$w_{interaction} = \frac{1}{\sigma}\int_0^{E_{max}} \frac{d\sigma}{dE} dE \tag{4.11}$$

Where $\sigma = \sigma_{pe} + \sigma_{cs}$ is the total cross-section of gamma-rays.

The last parameter that is constrained is the number of interactions a photon is allowed to have. Again, this restriction influences the simulation in two ways. Firstly the simulation forces the photons to interact as many times as desired. Secondly it influences the selection of the scatter process. When it is not the last interaction of the photon, the photo-electric effect is prohibited. When the last interaction is a Compton scatter, the photon is transported out of the volume in the same manner as the teleportation that is used to transport the gamma rays to the region of interest.

Chapter 5

Variance reduction techniques for Monte Carlo simulations of gamma-rays

In recent years dual-phase liquid xenon time projection chambers (TPCs) have managed to roughly double the sensitivity to WIMP recoils every year for the past decade [46]. New efforts are being made to build even bigger detectors to increase WIMP recoil sensitivity further. Besides a larger target volume, background control is of vital importance to such experiments. While internal backgrounds are lowered drastically, γ rays from the detector materials will remain a challenge in future detectors. Where the vast majority of the γ rays interact before entering the active part of the detector, a small fraction will penetrate and leave a background signal in the active region. Simulation of such rare events become increasingly computational expensive due to the increasing size of the LXe detectors. Variance reduction techniques can be utilized to increase the efficiency of such rare event simulations. These techniques allow to only sample events that lie within the region of interest for WIMP searches. As presented in this paper, such methods yield accurate results and are able to improve sensitivity by three orders of magnitude. Besides single scatter gamma-ray interactions, the VRT can also be used to increase the stimulation efficiency of multiple scatters and for neutron scatters studies.

Variance reduction techniques for Monte Carlo simulations of photon transport in liquid xenon detectors

S. Bruenner, A.P. Colijn, M.P. Decowski, O.V. Kesber

Prepared for submission to:
NUCLEAR INSTRUMENTS AND METHODS A

5.1 Abstract

Monte Carlo simulations are a crucial tool for the analysis and prediction of various background components in liquid xenon (LXe) detectors. With improving shielding properties of new experiments, the simulation of external backgrounds, such as induced by gamma rays from detector materials, gets more and more computational expensive. We introduce and validate an accelerated Monte Carlo simulation technique for photon transport in liquid xenon detectors. The method simulates photon-induced interactions within a defined geometry and energy range with high statistics while interactions outside of the region of interest (ROI) are not simulated directly but are taken into account by means of probability weights. For a simulation of gamma induced backgrounds in an exemplary detector geometry we achieve a three orders of magnitude acceleration compared to a standard simulation of a current current ton-scale LXe dark matter experiment.

5.2 Introduction

In the last decades, liquid xenon (LXe) detectors became a leading technology for rare event searches in astro particle physics. Many of the most stringent limits for the direct detection of dark matter [47, 48] or on the neutrinoless double-beta decay [49] have been set by LXe experiments. One major advantage of LXe is its high mass density and the resulting high self-shielding capability against external radiation. Background induced by gamma radiation from radioactive decays in detector materials is efficiently reduced in the central LXe volume due to the shielding of the outer xenon layers. In order to optimize the detector sensitivity, a precise knowledge of the remaining background components is essential. Therefore, many experiments do intensive measurements of trace radioactivity impurities in the detector materials [50, 51]. This data is used as input for Monte Carlo simulations of the gamma background in the central LXe volume [52, 53]. For future large scale detectors, employing up to 50 t of LXe [54], these simulations will become computationally expensive as a large number of gamma emissions need to be simulated in order to achieve a robust prediction of background events in the center of the detector, particularly in the low energy regime of a few tens of keV. Variance reduction techniques (VRT) such as *importance sampling* [55] are one approach to increase the precision of Monte Carlo simulations while at the same time reducing the computational effort.
In this paper, we introduce a VRT dedicated to the simulation of external gammas in LXe detectors. The statistical uncertainty is decreased with respect to standard Monte Carlo simulations by means of importance sampling. The simulation can be restricted to photon interactions in the region of interest (ROI) of a rare event signal. The underlying probability density functions (pdf) are thus over-sampled in the ROI, while they are not sampled in other regions of phase space. The non-sampled events are taken into account by applying corresponding weights to the obtained simulation result in the ROI. Section 2 introduces the VRT used for the following simulations in this paper. For validation, we simulate gamma interactions in LXe by means of the standard Monte Carlo approach and compare those to the VRT simulation results. A discussion of the achieved acceleration due to VRT is presented in section 3. We conclude with a summary of of our results in section 4.

5.3 Simulation Method and Validation

To study the variance reduction techniques proposed in this paper, we developed a photon transport Monte Carlo code in Python. It implements both a standard simulation technique and a variance reduction method to validate our acceleration techniques. During the photon transport only the photo-electric effect and Compton scattering are taken into account, with the mass attenuation coefficients μ as provided by NIST [56]. If a photo-electric absorption takes place, all the photon energy is assumed to be deposited locally and further tracking of the photo-electron is not done: this is a reasonable assumption since the photo-electrons will only traverse a distance of a few 100 μm in liquid xenon, which is below the position resolution of current LXe experiments [57]. In the case of a Compton scattering event, we use the Klein-Nishina differential cross-section to calculate the scattering angle, while taking into account the binding energy of electrons with appropriate form factors [58]. These form factors are especially important in the regime of low-energy deposits in the keV range, and thus for dark matter searches. The MC code does not take into account pair creation. Thus, its applicability is in principle limited to gamma ray energies below the pair creation threshold of 1.02 MeV. However, it is safe to assume that the actual results are reliable up to energies of ~ 1.5 MeV since the pair-production cross-section is about one order of magnitude below the incoherent cross-section.

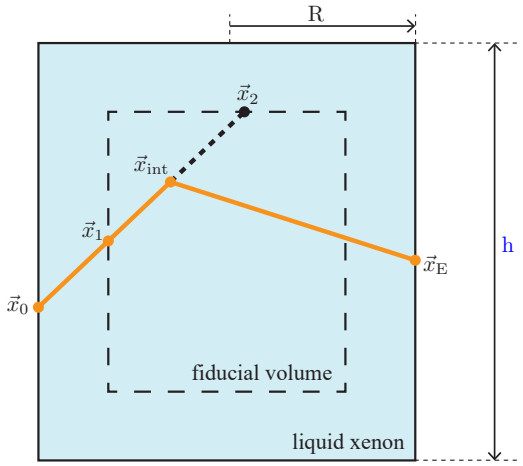

Figure 5.1 – Geometry for the simulation studies presented in this paper, representing a simplified dark matter experiment similar to XENONnT [**?**] or LZ [59]. Most high-energy gamma rays originate from the boundary of the liquid xenon volume, while signal events occur in the central fiducial volume (FV). The orange line represents a possible trajectory of a gamma ray through the liquid xenon, scattering once.

We use a cylinder with a radius of $R = 65$ cm and a height of $h = 150$ cm filled with 6 t of LXe as a benchmark model (see Figure 5.1). For simplicity, the detector walls or other detector components were not assumed to be present. Gamma rays can be emitted from random locations on the cylinder's surface. The fiducial volume (FV) is a cylinder with a radius of 57 cm and a height of 134 cm at the center of the xenon volume, such that it is surrounded by 8 cm of LXe on all sides. Such a geometry mimics dark matter detector like for example LZ [59] or XENONnT [**?**]. It has to be noted, however, that given the simplicity of the geometry this study should only be viewed as a feasibility and validation study of the acceleration technique discussed below.

5.3.1 Variance Reduction Technique

A simulated gamma ray with a certain primary position and direction of propagation has a probability p_γ to create an interaction in the pre-defined FV and energy region. Obviously p_γ is dependent on the gamma ray's initial parameters. We factorize the event probability as

$$p_\gamma = \prod_{i=1}^{4} p_i \cdot p_s \quad , \tag{5.1}$$

where the probabilities p_i correspond to well-described processes such as the adsorption probability of a photon when traveling through LXe. We will introduce and discuss those processes, four in total, later in this section. p_s, on the other hand, is the combined probability for other processes which are not explicitly taken into account. Instead of determining p_i by means of simulation, as it is done in a standard MC approach, we calculate them for each created gamma on an event-by-event base. As a consequence, the probability for a simulated gamma to induce an interaction in the ROI is increased to $p_\gamma = p_s$ since the processes described by p_i will not terminate the simulated event. Instead they act as a weight on the events simulated in the ROI to retain the correct p_γ from equation 5.1. The probability weights p_i refer to different photon transport or interaction processes and are determined as follows.
A gamma ray pointing towards the direction of the FV has a probability p_1 to be transported to the edge of the FV, $\vec{x}_1$ in Figure 5.1, without undergoing an interaction. p_1 is

dependent on the path length $|\vec{x}_1 - \vec{x}_0|$ and is calculated as

$$p_1 = \exp\left(-\rho\ \mu(E_\gamma)\,|\vec{x}_1 - \vec{x}_0|\right) \quad , \tag{5.2}$$

where ρ is the density of LXe ($\sim 3\mathrm{g/cm}^3$) and $\mu(E_\gamma)$ is the mass attenuation coefficient. Once the gamma ray reaches the FV, it has a probability p_2 to undergo an interaction before leaving the sensitive volume at position $\vec{x}_2$. In the accelerated simulation, we force an interaction in the FV and apply the weight

$$p_2 = 1 - \exp\left(-\rho\,\mu(E_\gamma)\,|\vec{x}_2 - \vec{x}_1|\right) \quad . \tag{5.3}$$

Simulations in the low energy region are particularly computationally expensive. We can accelerate the simulation by restricting the interactions to energies smaller than a maximum energy deposit of E_{max}. The photo-electric effect is prohibited if the energy of a gamma is larger than E_{max} and for Compton scattering only scattering angles associated with interactions below the maximum energy are allowed. Simulated interactions need to be weighted by the probability for an interaction below E_{max} which is given by

$$p_3 = \frac{1}{\sigma}\int_0^{E_{max}} \frac{d\sigma}{dE} dE \quad , \tag{5.4}$$

where $\sigma = \sigma_{pe} + \sigma_{cs}$ is the total cross-section of gamma-rays including the photo-electric effect and Compton scattering, respectively. Finally, in order to produce a single scatter event the gamma needs to leave the sensitive volume without any further energy deposition. The corresponding probability is calculated similarly to Eq. 5.2 by

$$p_4 = \exp\left(-\rho\ \mu(E_\gamma)\,|\vec{x}_E - \vec{x}_{int}|\right) \quad . \tag{5.5}$$

We restricted the discussion so far to an event topology where the gamma leaves the LXe volume after a single interaction. However, the introduced acceleration methods can be easily extended to multiple interaction events as we will discuss later. In that case the probability weights are adapted to a gamma undergoing a certain number of interactions within the pre-defined energy range and then leaving the FV or getting terminated in the last interaction by photo-electric absorption.

5.3.2 Validation

In order to validate our accelerated simulation method, we compare the results with those obtained from a standard MC simulation. To simplify the discussion, we use the simulation of single scatter events induced by mono-energetic gamma rays of 1 MeV as an example. In the first validation step we did not define a FV. This means the weights for transportation until the FV and for the maximum energy deposition are unity, i.e., $p_1 = p_3 = 1$. The obtained energy spectra of the standard MC method and the accelerated simulation are shown in Figure 5.2. Both show excellent agreement with each other in their prediction of the intensity of the photo-peak at 1 MeV and the Compton spectrum. This proves that the physics of gamma interactions is implemented in a consistent way among the simulation methods. In the second step we compare the energy spectra of single scatter interactions within a FV which is shielded by 8 cm of LXe on all sides. The calculated weight p_1 is used in the accelerated simulation. The spectrum of the standard MC suffers from very low statistics apart of the photo-absorption peak (see Figure 5.2). The accelerated MC, in contrast, obtains a clear spectrum with high statistics since no initial gamma gets terminated on its way to the FV. Both spectra agree with each other after applying all weights to the accelerated MC. The decreasing shape of the Compton spectrum is explained by the single scatter requirement and reflects the decreasing probability of a gamma to

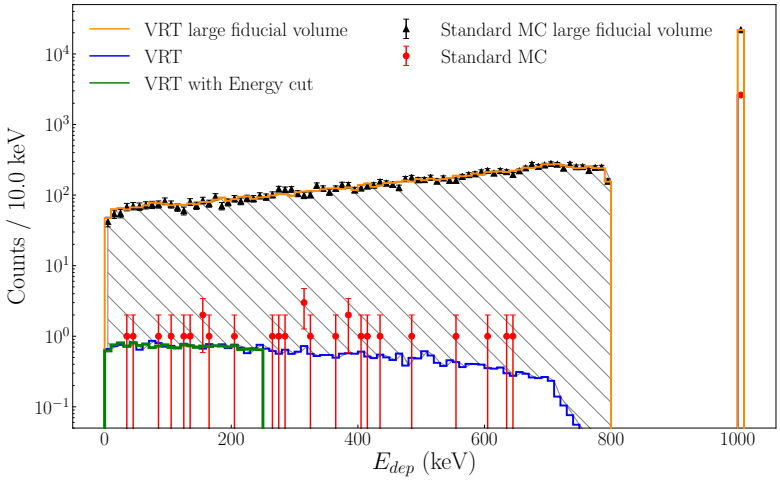

Figure 5.2 – The energy spectra of single scatter events originating of 10^6 simulated gamma-rays of 1 MeV energy. Results obtained with the standard MC methods without/with a fiducial volume (FV) are indicated by black/red markers, respectively. The accelerated simulation spectra, indicated by colored histograms, are in agreement with the standard MC but have higher statistics in the FV.

escape the detector without any further interactions as a function of the gamma's first energy deposition. The third test is an accelerated MC simulation with a maximum energy requirement of $E_{max} = 250\,\text{keV}$. The fact that it is in agreement with the previous simulation without an energy cut-off is a validation of the weight p_3 in the accelerated simulation.
As a figure of merit, we can predict the number of gamma induced background events N_{BG} in the FV using the standard MC and the accelerated MC approach with increasing statistics. We use an accelerated MC simulation of 10^9 events and its expectation value μ_{BG} as a reference simulation. Figure 5.3 shows that the standard MC expectation value of events within the FV (no energy cut applied) converges to the reference value with increasing number of simulated gammas N_γ. The error on the standard MC is obtained by $\sqrt{N_{BG}}/\mu_{BG}$ since the error on the reference MC is negligible. For comparison we also show the accelerated MC simulation (blue marker) which converges much faster to the reference value. The error on the accelerated MC is determined from the variance of 10 simulations as we will discuss below.
Both validation studies, on the spectral shape as well as on the absolute number of simulated background events in a FV, show good agreement between the standard MC and the accelerated simulation.

5.4 Acceleration factor

As described in Section 5.3.1, our method gains its acceleration by accounting for some photon transport and physics processes by means of weights p_i instead of determining those survival probabilities for an event to happen in the ROI by simulation. The increased sampling in the ROI leads to a more precise expectation value of the simulation, i.e., with a smaller standard deviation for a given number of simulated gammas. This section quantifies the acceleration of our method compared to the standard MC method by determining the number of events for both simulations that yield the same statistical uncertainty on the estimated events in the ROI. This acceleration will depend on the

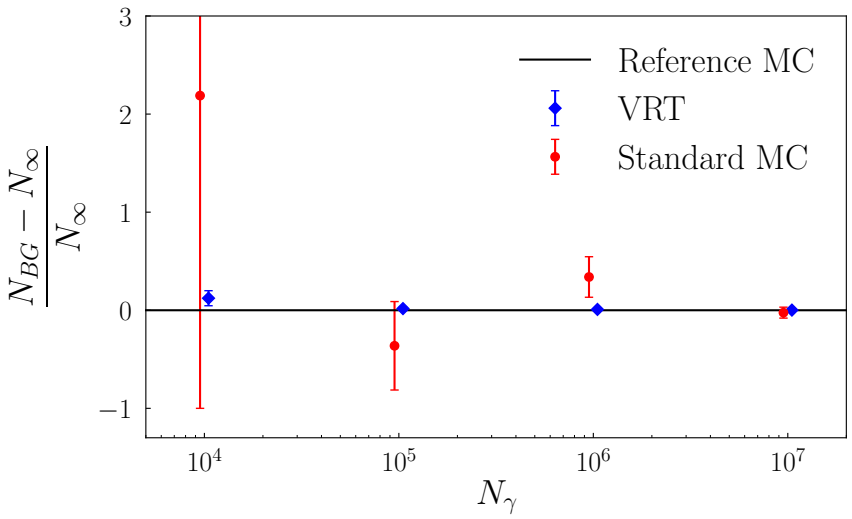

Figure 5.3 – The relative difference between the predicted number of interactions, N_{BG}, and the expected number N_∞, obtained in a high statistic accelerated MC. The standard MC prediction (red) converges to N_∞ for a large number of simulated events N_γ but slower than the accelerated MC (blue).

detector geometry and energy of the gamma rays, but it is independent of computing power.

To quantify the acceleration we perform for both MC methods a set of 10 independent simulations with a certain number of initial gammas N_γ at 1.5 MeV. The goal is to determine the expected number of single-scatter events N_{BG} within a defined FV. For these simulations the detector geometry and FV were fixed as shown in Figure 5.1 and an energy cut was set to $E_{max} = 250\,\text{keV}$. The results obtained for four different N_γ are shown in Figure 5.4. In all cases we observe that the expectation values N_{BG} obtained by the standard MC method for a certain N_γ have a much larger spread than the results from the acceleration method. For both methods the mean, $\bar{N}_{MC}$ and $\bar{N}_{VRT}$ respectively, converges to the expectation value of a high statistics reference simulation referred to as N_∞. However, the sample variance σ_{MC} for the standard MC is much larger with respect to σ_{VRT} in the accelerated simulation.

Figure 5.5 depicts the evolution of the relative undertainty $\sigma/\bar{N}$ as a function of the number of simulated events for the standard MC and the VRT MC. For the simulations with $N_\gamma < 10^4$ no interaction happened in the ROI in the standard MC approach. The same relative error is achieved with a smaller number of simulated events for the accelerated MC, due to the more efficient sampling of the underlying probability density functions in the ROI. For both simulations the dependence of the relative statistical uncertainty on N_γ is parameterized as

$$\sigma/\bar{N} = \frac{c}{\sqrt{N_\gamma}} \quad . \tag{5.6}$$

The fit model provides only a qualitative description of the data. Nevertheless we use the fit-parameters to estimate the achieved acceleration for a particular simulation geometry. The acceleration factor, α, is defined as the ratio of the number of events using the accelerated MC, N_γ^{VRT}, and the standard MC N_γ^{MC}, when both methods achieve a certain relative statistical uncertainty, i.e.,

$$\alpha = \frac{N_\gamma^{VRT}}{N_\gamma^{MC}} = \left(\frac{c^{MC}}{c^{VRT}}\right)^2 \tag{5.7}$$

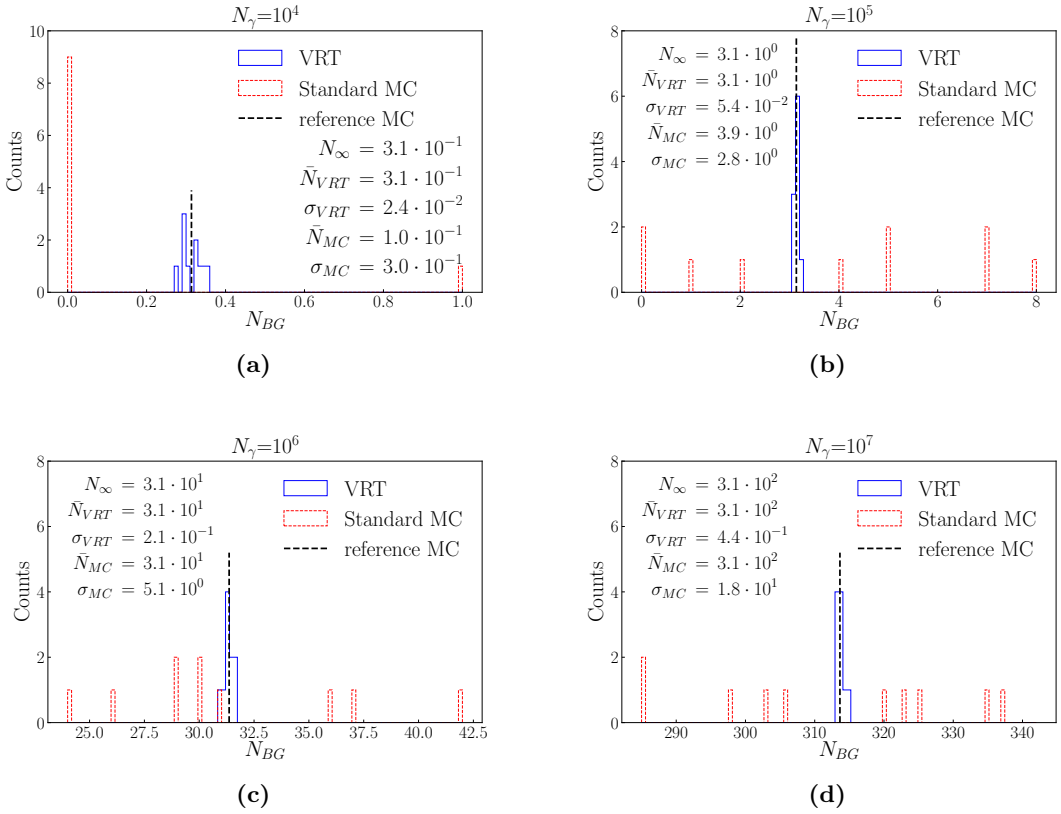

Figure 5.4 – The number of gamma rays undergoing a single scatter inside the fiducial volume with an energy deposit of $< 250\,\mathrm{keV}$. Figures a-d, show the simulation results for an initial number of gamma rays of 10^4, 10^5, 10^6 and 10^7, respectively. As a reference serves the expectation value N_∞ from a high statistics simulation. In case of the accelerated method the expectation value of the predicted number of interactions in the ROI, $\bar{N}_{VRT}$, shows a much reduced variance, σ_{VRT}, with respect to the standard MC approach.

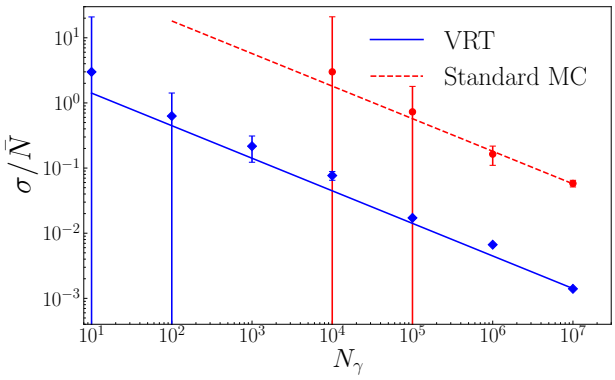

Figure 5.5 – Evolution of the relative sample variance as a function of N_γ for the standard MC (red) and VRT MC (blue). The lines correspond to a fit of equation 5.6 to the datapoints.

with c^{MC} and c^{VRT} the fitted slopes from equation 5.6. In our particular geometry we achieve an acceleration factor of 1800 for single scatter events in the ROI. Due to the multidimensionality of a Monte Carlo simulations it is impossible to predict in advance what the acceleration factor will be. It strongly depends on the particulars of the chosen geometry and the energy of the gamma rays. The acceleration technique will generally benefit the simulation of extremely rare events due to the efficient sampling of the underlying pdf in the ROI.

5.5 Discussion and Conclusion

This paper presents the proof of principle for a variance reduction technique that can be used to estimate gamma ray backgrounds in large Dark Matter experiments. The evaluation of the method showed an acceleration factor $\alpha = 1800$ with respect to a standard non-weighted Monte Carlo simulation. The acceleration factor will depend on the geometry of the system, the size of the fiducial volume, and the energy of the gamma rays. As a general rule of thumb, the larger the detector volume, the larger α becomes, due to the fact that the survival probability of the gamma rays decreases exponentially with increased pathlength. Similarly, the maximal allowed energy deposition has a strong impact on the achieved acceleration factor. If the cut-off is at low energy deposits, as in the signal-region for WIMP nuclear recoils, the acceleration factor is large, as simulation of not contributing photo-electric absorption events is eliminated. Furthermore, we observed that α varied by a factor of ~ 3 over the energy range of 500 keV to 1.5 MeV, due to strong variation of the photo-electric and incoherent cross-sections.

One important aspect of simulations for WIMP detection experiments is the capability to simulate neutrons, since these may cause an irreducible background. For this proof of principle study we chose to simulate gamma rays only, since the physics processes relevant to their transport is relatively simple. The same acceleration method is applicable to neutron transport as well and could be implemented using e.g. GEANT4 [60].

Closely related to the capability to simulate neutrons, is the ability to simulate multiple-scatter events. Neutrons, in sharp contrast to WIMPs, have a sizeable probability to undergo a double scatter, and it is therefore of crucial importance to acquire detailed knowledge of such events. Although we quantified the acceleration factor for single scatter events only, the simulation code is set-up to simulate multiple-scatters. Figure 5.6 shows the spatial distribution of single and double scattered 1 MeV gamma rays for both the standard Monte Carlo and for the accelerated simulation. Both interactions were required to happen inside the fiducial volume, while the total energy deposit was required to be below 250 keV. For the standard Monte Carlo only very few events are accepted, resulting in a relatively high uncertainty on this background, whereas the accelerated Monte Carlo shows a smooth distribution of events. Besides offering a much more precise estimate of this background, this also allows to investigate the details of such events. For example, based on the accelerated simulation it is possible to clearly identify which detector components contribute significantly to the background, and take these results into consideration in the detector design.

To summarize, a new variance reduction technique for photon transport was developed and validated. Much faster estimates of backgrounds can be obtained, and this method has the potential to accelerate simulations for neutron background estimates and multiple scatter events allowing their study in much greater detail.

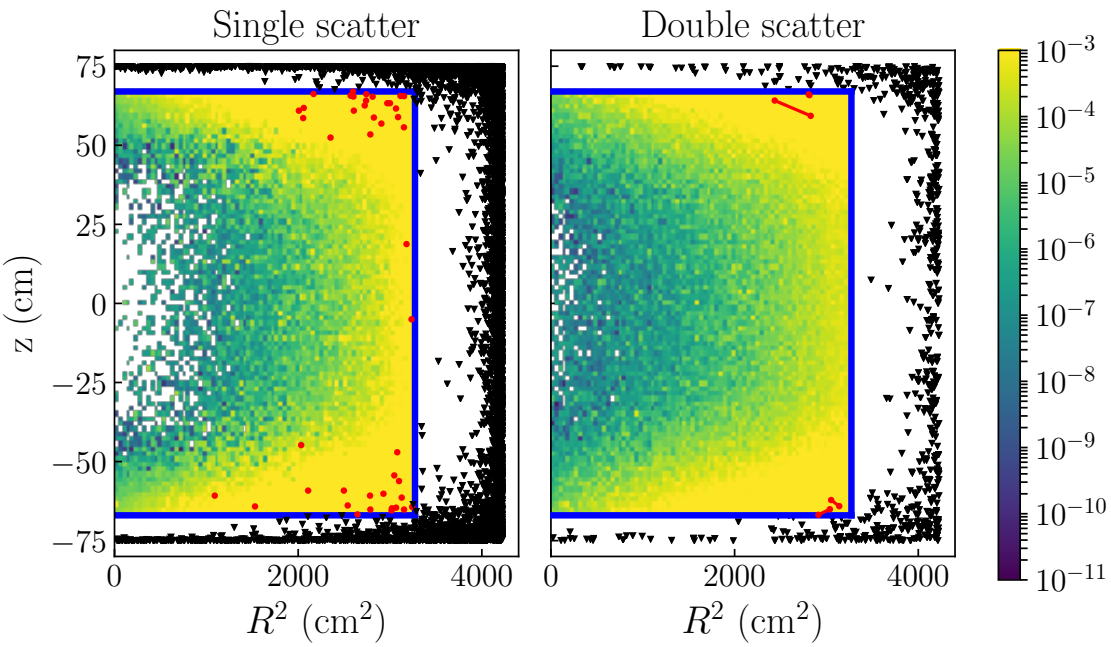

Figure 5.6 – Spatial distribution of single scatter (left) and double scatter events (right) from a simulation of 10^6 gamma rays of 1 MeV energy. The maximum total energy deposit in the target is below 250 keV. The dots represent the energy deposits from the standard Monte Carlo, while the colored distribution shows the energy deposits from the accelerated simulation inside the FV. For the double scatter events simulated with the standard MC the red lines are connecting the first and second scatter inside the FV. The standard MC gives sparse information inside the FV both for single scatters and for double scatters. The accelerated MC gives a more detailed - low variance - estimate of the spatial distribution of the background events.

Chapter 6

Conclusions and outlook

6.1 Conclusions and outlook

From astronomical observations, there is striking evidence that our laws our gravity are either incorrect or that there is a 25% of the mass in the universe consist of an unknown substance. If one goes by the later, the question arises what this substance can possibly be. One of the prime candidates is called the WIMP. Measuring a WIMP would mean a major breakthrough in modern physics. Therefore experiments like XENONnT and DARWIN will try to directly measure the interaction of a WIMP with a xenon nucleus. Because the proposed interaction rate of WIMPS is in the order of single events background control is of major importance. One of these backgrounds arises from radioactive decays of materials in the detector. These decays can produce gamma-rays that penetrate into the active part of the detector. These rays can leave a background signal. However, since the self-shielding properties of LXe, such backgrounds only happen ~ 1 for every two million created photons. Due to this low probability simulations struggle to give a precise estimate of such backgrounds. A variance reduction technique called important sampling can improve the simulation efficiency and therefore produce a better estimate on the number of background events in such an area.

In chapter 5, a VRT is presented that aims to improve statistics on rare gamma-ray background events. This improvement is achieved by constraining the parameter space of the interactions to the interaction location, max energy deposit and the number of interactions. Weights are applied to the events in order to account for the sampling biases. Using this method will yield an accurate background estimate with respect to a normal simulation and with respect to a large reference simulation. On terms of precision, the VRT outperforms a normal simulation by a factor of 10^3. However, this figure of merit is highly dependant on the simulation characteristics and therefore can be higher for more exceptional events like double scatters or scatters within a smaller fiducial volume. Besides gamma-rays, the VRT can be used to simulate neutron scatters. These extensions applications of the VRT are topics of other studies.

6.2 Acknowledgements

The last year has been an incredible experience. It has been, insightful, fun and inspiring thanks to the great mix of people that helped me with this project. I want to thank Auke-Pieter Colijn for giving me the possibility to start on this project. I really enjoyed the meetings we have had over the past year and learned a great deal about how to actually do experimental physics, and you reminded me always to understand the microphysics. Furthermore, it was a great experience assist in teaching the essence of Dark matter research to my fellow master students. Besides Auke-Pieter I thank Stefan Bruenner for besides being a great supervisor also showed us around in Grand Sasso. Furthermore, the weekly runs were always a good possibility to clear the mind. I thank Patrick Decowski for being welcomed in the NIKHEF Dark Matter group. The level of engagement of students in all kind of activities is something I especially enjoyed. I thank Peter, Joran and Alvaro for the insightful feedback and showing me around at NIKHEF and in the academic world in general. I have enjoyed working alongside my fellow students Davey, Thomas, Bouke, Lucas, Gijs, Leonore, Isis Patrick, Frederick, Brit, Mehmet and Marieke, the ping-pong sessions were some of the best breaks one could wish for. Furthermore, I thank Jim Carstens and my brother Boris for their help and support of the work. Mom and Dad, my thanks to you, is great, and I am grateful for such supportive parents. Lastly, my biggest thanks goes to Marloes her endless support and advice. Your endless positivity was the best distraction and provided me with the motivation to complete this project.

Bibliography

[1] P. A. R. Ade et al. Planck2013 results. xvi. cosmological parameters. *Astronomy Astrophysics*, 571:A16, Oct 2014.

[2] Robert J. Nemiroff and Bijunath Patla. Adventures in friedmann cosmology: A detailed expansion of the cosmological friedmann equations. *American Journal of Physics*, 76(3):265–276, 2008.

[3] P. A. R. Ade, N. Aghanim, M. Arnaud, M. Ashdown, J. Aumont, C. Baccigalupi, A. J. Banday, R. B. Barreiro, J. G. Bartlett, and et al. Planck2015 results. *Astronomy Astrophysics*, 594:A13, Sep 2016.

[4] Constantinos Skordis. The tensor-vector-scalar theory and its cosmology. *Classical and Quantum Gravity*, 26(14):143001, jun 2009.

[5] Xiao-dong Xu, Bin Wang, and Pengjie Zhang. Testing the tensor-vector-scalar theory with the latest cosmological observations. *Phys. Rev. D*, 92:083505, Oct 2015.

[6] E. Hogenbirk. *A spark in the dark*. PhD thesis, Universiteit van Amsterdam, 3 2019.

[7] Olivier Kesber. Github fast mc. :/github.com/Olkes/Gamma-ray_FastMC, 2020.

[8] Volker Springel, Carlos S. Frenk, and Simon D. M. White. The large-scale structure of the universe. *Nature*, 440(7088):1137–1144, 2006.

[9] Peter Schneider. Mapping the dark matter with weak gravitational lensing. pages 51–58, 1999.

[10] Douglas Clowe et al. A direct empirical proof of the existence of dark matter. *The Astrophysical Journal*, 648(2):L109âL113, Aug 2006.

[11] Chandra, nasa finds direct proof of dark matter :: 1e 0657-56 :: 21 aug 06.

[12] A.P. Colijn. Experimental quantum physics: Dark matter, November 2016.

[13] Edvige Corbelli and Paolo Salucci. The extended rotation curve and the dark matter halo of M33. *Monthly Notices of the Royal Astronomical Society*, 311(2):441–447, 01 2000.

[14] Gianfranco Bertone, Dan Hooper, and Joseph Silk. Particle dark matter: evidence, candidates and constraints. *Physics Reports*, 405(5):279 – 390, 2005.

[15] Gianfranco Bertone and Tim M. P. Tait. A new era in the search for dark matter. *Nature*, 562(7725):51â56, Oct 2018.

[16] Mirco Cannoni. Exact theory of freeze-out. *The European Physical Journal C*, 75(3), Mar 2015.

[17] Erik Verlinde. Emergent gravity and the dark universe. *SciPost Physics*, 2(3), May 2017.

[18] Georg G. Raffelt. Astrophysical axion bounds. *Axions*, page 51â71.

[19] Alexey Boyarsky, Oleg Ruchayskiy, and Mikhail Shaposhnikov. The role of sterile neutrinos in cosmology and astrophysics. *Annual Review of Nuclear and Particle Science*, 59(1):191â214, Nov 2009.

[20] C. Alcock, R. A. Allsman, D. R. Alves, T. S. Axelrod, A. C. Becker, D. P. Bennett, K. H. Cook, N. Dalal, A. J. Drake, K. C. Freeman, and et al. The macho project: Microlensing results from 5.7 years of large magellanic cloud observations. *The Astrophysical Journal*, 542(1):281â307, Oct 2000.

[21] B. P. Abbott et al. Observation of gravitational waves from a binary black hole merger. *Phys. Rev. Lett.*, 116:061102, Feb 2016.

[22] M. Aaboud, G. Aad, B. Abbott, J. Abdallah, O. Abdinov, B. Abeloos, R. Aben, O.âS. AbouZeid, N.âL. Abraham, H. Abramowicz, and et al. Search for new phenomena in final states with an energetic jet and large missing transverse momentum inppcollisions ats=13ââtevusing the atlas detector. *Physical Review D*, 94(3), Aug 2016.

[23] Teresa Marrodán Undagoitia and Ludwig Rauch. Dark matter direct-detection experiments. *Journal of Physics G: Nuclear and Particle Physics*, 43(1):013001, Dec 2015.

[24] P. Brun. Indirect searches for dark matter with ams-02. *The European Physical Journal C*, 56(1):27â31, Jun 2008.

[25] Francis Halzen and Dan Hooper. The indirect search for dark matter with icecube. *New Journal of Physics*, 11(10):105019, Oct 2009.

[26] T. K. Gaisser, G. Steigman, and S. Tilav. Limits on cold-dark-matter candidates from deep underground detectors. *Phys. Rev. D*, 34:2206–2222, Oct 1986.

[27] Fermi-LAT Collaboration. Characterizing the population of pulsars in the inner galaxy with the fermi large area telescope, 2017.

[28] D. S. Akerib et al. Projected wimp sensitivity of the lux-zeplin dark matter experiment. *Physical Review D*, 101(5), Mar 2020.

[29] E. Aprile et al. Dark matter search results from a one ton-year exposure of xenon1t. *Phys. Rev. Lett.*, 121:111302, Sep 2018.

[30] E. Aprile, et al. Constraining the spin-dependent wimp-nucleon cross sections with xenon1t. *Phys. Rev. Lett.*, 122:141301, Apr 2019.

[31] J. Aalbers et al. Darwin: towards the ultimate dark matter detector. *Journal of Cosmology and Astroparticle Physics*, 2016(11):017â017, Nov 2016.

[32] G Bellini, J Benziger, D Bick, G Bonfini, D Bravo, M. Buizza Avanzini, B Caccianiga, L Cadonati, F Calaprice, C Carraro, and et al. Cosmic-muon flux and annual modulation in borexino at 3800 m water-equivalent depth. *Journal of Cosmology and Astroparticle Physics*, 2012(05):015â015, May 2012.

[33] E. Aprile et al. The xenon1t dark matter experiment. *The European Physical Journal C*, 77(12):881, 2017.

[34] J. Aalbers. *Dark matter search with XENON1T*. PhD thesis, Universiteit van Amsterdam, 6 2018.

[35] G.F. Knoll. *Radiation Detection and Measurement*. Wiley, 2010.

[36] E. Aprile, et al. Physics reach of the XENON1t dark matter experiment. *Journal of Cosmology and Astroparticle Physics*, 2016(04):027–027, apr 2016.

[37] L. Baudis, A. Ferella, A. Kish, A. Manalaysay, T. Marrodán Undagoitia, and M. Schumann. Neutrino physics with multi-ton scale liquid xenon detectors. *Journal of Cosmology and Astroparticle Physics*, 2014(01):044–044, jan 2014.

[38] Wolfram Research, Inc. Mathematica, Version 12.1. Champaign, IL, 2020.

[39] J. B. Albert, M. Auger, D. J. Auty, P. S. Barbeau, E. Beauchamp, D. Beck, V. Belov, C. Benitez-Medina, J. Bonatt, M. Breidenbach, and et al. Improved measurement of the$2\hat{\nu}\hat{\beta}\hat{\beta}^2\hat{\nu}^2 half - life of 136 xe with the exo - 200 detector. Physical Review C, 89(1), Jan 2014.$

[40] Xcom photon cross sections database, 2010. retrieved on April 1, 2019, `https://www.nist.gov/pml/xcom-photon-cross-sections-database`.

[41] Stefan Augustin BrÃ¼nner. *Mitigation of ^{222}Rn induced background in the XENON1T dark matter experiment*. PhD thesis, U. Heidelberg (main), 2017.

[42] Shingo Kazama. The xenonnt neutron veto detector. URL: `http://www-kam2.icrr.u-tokyo.ac.jp/indico/event/3/session/40/contribution/298/material/slides/0.pdf`, 9 2019.

[43] G. Nelson and D. Rewy. Gamma-ray interactions with matter, 1991.

[44] Arthur H. Compton. A quantum theory of the scattering of x-rays by light elements. *Phys. Rev.*, 21:483–502, May 1923.

[45] J. H. Hubbell. Atomic form factors, incoherent scattering functions, and photon scattering cross sections. *Journal of Physical and Chemical Reference Data*, 4(3):471–538, 1975.

[46] Laura Baudis. Wimp dark matter direct-detection searches in noble gases. *Physics of the Dark Universe*, 4:50 – 59, 2014. DARK TAUP2013.

[47] E. Aprile et al. Dark Matter Search Results from a One Tonne x Year Exposure of XENON1T. *Phys. Rev. Lett.*, 121:111302, 2018.

[48] D. S. Akerib et al. Projected wimp sensitivity of the lux-zeplin dark matter experiment. *Phys. Rev. D*, 101:052002, Mar 2020.

[49] G. Anton et al. Search for neutrinoless double-β decay with the complete exo-200 dataset. *Phys. Rev. Lett.*, 123:161802, Oct 2019.

[50] E. Aprile et al. Material radioassay and selection for the xenon1t dark matter experiment. *The European Physical Journal C*, 77(12):890, 2017.

[51] D.S. Akerib et al. The LUX-ZEPLIN (LZ) radioactivity and cleanliness control programs. 6 2020.

[52] E. Aprile et al. Physics reach of the XENON1T dark matter experiment. *JCAP*, 1604(04):027, 2016.

[53] D.S. Akerib et al. Radiogenic and muon-induced backgrounds in the lux dark matter detector. *Astroparticle Physics*, 62:33 – 46, 2015.

[54] J. Aalbers et al. DARWIN: towards the ultimate dark matter detector. *JCAP*, 2016(11):017–017, nov 2016.

[55] Surya T. Tokdar and Robert E. Kass. Importance sampling: a review. *WIREs Computational Statistics*, 2(1):54–60, 2010.

[56] Xcom photon cross sections database, 2010. retrieved on April 1, 2019, `https://www.nist.gov/pml/xcom-photon-cross-sections-database`.

[57] E. Aprile et al. XENON1T Dark Matter Data Analysis: Signal Reconstruction, Calibration and Event Selection. *Phys. Rev. D*, 100(5):052014, 2019.

[58] J. H. Hubbell et al. Atomic form factors, incoherent scattering functions, and photon scattering cross sections. *Journal of Physical and Chemical Reference Data*, 4(3):471–538, 1975.

[59] D.S. Akerib et al. The LUX-ZEPLIN (LZ) Experiment. *Nucl. Instrum. Meth. A*, 953:163047, 2020.

[60] S. Agostinelli et al. Geant4âa simulation toolkit. *Nuclear Instruments and Methods in Physics Research Section A: Accelerators, Spectrometers, Detectors and Associated Equipment*, 506(3):250 – 303, 2003.